# A radio view of dust-obscured star formation

Vlugt, D. van der

# 5 | ALMA confirms optically dark population at $z > 3$


## Abstract

Using ALMA spectral scan observations covering 84–108 GHz, we report observations of 10 radio-selected star-forming galaxies at $z \gtrsim 3$ in the COSMOS field which are unseen in deep imaging from the ultraviolet to the near-infrared. With the addition of an archival and a recent additional ALMA observation for two of the sources, we securely detect CO emission lines in eight sources. For the other two sources, we find tentative line detections. The redshifts are unambiguously identified for six sources. The remaining four sources have two possible redshift solutions, and we use the $L'_{\mathrm{CO(5\text{-}4)}}$–$\mathrm{L_{IR}}$ correlation to identify the most likely redshift solution for each source. We find that the redshifts of the observed sources lie between $z = 3.1$ and $z = 5.0$, with a median redshift of $z = 3.95 \pm 0.62$. This confirms that the 'optically dark' sources targeted lie at $z \gtrsim 3$. We derive that the 'optically dark' sources contribute $5.42 \pm 0.41 \times 10^{-4}\,\mathrm{M_\odot yr^{-1} Mpc^{-3}}$ to the cosmic star formation rate density at $z \sim 4$ and show that it validates some previous estimates relying on photometric redshifts. This study confirms the cosmic importance of these sources at high ($z > 3$) redshift.




van der Vlugt, Jin, Hodge, Algera
*to be submitted to The Astrophysical Journal*

## 5.1 Introduction

For the last 20 years, our knowledge of galaxy evolution has been based mainly on ultraviolet (UV) selected galaxy populations such as, e.g., Lyman-break galaxies (LBGs; Steidel et al. 1996) observed with deep surveys with the Hubble Space Telescope (*HST*). The Lyman break selection is biased towards young star-forming galaxies (SFGs) with little dust attenuation, leading to a significant number of dusty SFGs at high redshift missed by rest-frame UV surveys (e.g., Wang et al. 2009; Franco et al. 2018; Smail et al. 2021). This means measurements of the cosmic star formation rate density (SFRD) well beyond the era of peak galaxy assembly ($1 \lesssim z \lesssim 3$) (e.g, Bouwens et al. 2020) are biased against galaxies with significant dust obscuration (e.g., Madau & Dickinson 2014).

The discovery of sub-millimeter galaxies (SMGs) (e.g., Downes et al. 1999; Smail et al. 1999; Frayer et al. 2004) highlighted the importance of a more complete census of the star formation history across cosmic time. Since these galaxies are heavily attenuated in the rest-frame UV (e.g., Simpson et al. 2014; Franco et al. 2018; Dudzevičiūtė et al. 2020), they are generally missed in LBGs studies. Via high angular resolution Atacama Large Millimeter/sub-millimeter Array (ALMA) observations, we can now uncover faint SMGs missed by UV/optical-surveys: also classified as 'optically dark' sources (e.g., Gruppioni et al. 2020; Gómez-Guijarro et al. 2022; Shu et al. 2022; Xiao et al. 2023). Different observational studies conducted with ALMA have reached varying conclusions about the relative contribution of 'optically dark' population to the cosmic SFRD. For example, Franco et al. (2018) found that $20\% \pm 10\%$ of the 1.1mm sources are not detected with *HST* down to a depth of $H \sim 28$ mag. However, Wang et al. (2019) and Gruppioni et al. (2020) determined that the contribution of their 'dark' samples ranged from, respectively, $10^{+2.3}_{-5.1}$ % of the SFRD contributed by LBGs at similar redshifts, to almost equal ($48\% \pm 37\,\%$) to the total extinction-corrected contribution from all the known UV-selected galaxies at $z \sim 5$. Recently, observations of 'optically dark' sources have also been conducted with James Webb Space Telescope (*JWST*; Barrufet et al. 2023; Pérez-González et al. 2023), determining that these sources are mostly dusty star-forming galaxies and finding a similar contribution ($\sim 10\,\%$) to the SFRD as determined by Wang et al. (2019). Some of the discrepancy in the derived contributions to the SFRD may be due to the different methods of selecting the various optical/UV 'dark' samples.

Radio surveys are also powerful tools to help uncover the nature and contribution to the SFRD of 'optically dark' sources. Radio observations have been shown to identify 'optically dark' galaxies that contribute most significantly to the cosmic SFRD (Talia et al. 2021; Enia et al. 2022). Radio synchrotron emission provides a complementary way to trace star formation owing to its insensitivity to dust obscuration and strong correlation with far-infrared (FIR) emission and star formation rate (SFR) (FIR-radio correlation; e.g., Helou et al. 1985; Delvecchio et al. 2021) although it lacks the benefit of the negative K-correction in the FIR/sub-millimeter (sub-mm). In addition, radio observations offer high spatial resolution over larger areas than interferometric sub-mm observations. However, one of the major uncertainties in all of the above mentioned studies, including the radio-based studies, is the lack of reliable redshifts. For example, Talia et al. (2021) used the photometric redshift derived from

a stacked SED for 50% of their radio selected sample from the VLA-COSMOS 3 GHz Large Project (Smolčić et al. 2017a).

Recently, the COSMOS-XS survey has been carried out in the COSMOS field over an area of ∼350 arcmin$^2$ at 3 GHz (van der Vlugt et al. 2021). Since the study by van der Vlugt et al. (2021), the COSMOS-XS pointing has been additionally observed with the VLA L-band (1.4 GHz; Algera et al. in prep.). The ultra-deep, multi-band COSMOS-XS survey has been matched with the extensive multi-wavelength data in the COSMOS field (Algera et al. 2020a), enabling improved constraints on the radio-derived SFRD (van der Vlugt et al. 2022). The multi-wavelength matching of the COSMOS-XS data has also revealed a population of radio-detected 'optically dark' sources. van der Vlugt et al. (2023) showed the contribution of the 'optically dark' galaxies to the radio SFRD to be $\sim 15^{+7}_{-7}\%$ at $z \sim 5$, and they improved on previous studies (e.g., Talia et al. 2021; Enia et al. 2022) by making use of the new Super-deblended FIR-derived redshifts for sources with high $S/N_{FIR}$. The FIR-based redshifts suggested that these sources all lie at $z > 2$. However, they still had a significant uncertainty due to the redshift–$T_{dust}$ degeneracy (e.g., Pope & Chary 2010).

In this paper, we present ALMA follow-up observations of 10 $S_{1.1mm} > 3.5$ mJy 'optically dark' sources in the COSMOS-XS survey observed over the L-band area. Following van der Vlugt et al. (2023), the redshifts for these sources have been determined using the Super-deblending technique (Liu et al. 2018; Jin et al. 2019). With the follow-up observations, we are then able to use a blind line scanning technique with to derive their spectroscopic redshifts. Finally, we place constraints on the relative contribution of such 'optically dark' sources to the cosmic SFRD. Throughout this paper, the spectral index, $\alpha$, is defined as $S_\nu \propto \nu^\alpha$, where $S_\nu$ is the source flux density, and $\nu$ is the observing frequency. We use a ΛCDM cosmology with parameters $H_0 = 70\,\mathrm{km\ s^{-1}Mpc^{-1}}$, $\Omega_m = 0.3$, $\Omega_\Lambda = 0.7$ (Bennett et al. 2013). We assume a radio spectral index of −0.7 unless otherwise stated. We assume the Chabrier (2003) initial mass function (IMF) to calculate SFRs.

## 5.2 Data and sample selection

### 5.2.1 Selection of dark sources

The sample consists of 10 'optically dark' radio & sub-mm-bright sources, which were selected via three criteria: (1) covered by the primary beam (0.48 deg$^2$) of the COSMOS-XS L-band image and detected in either COSMOS-XS or JVLA-COSMOS 3 GHz images (van der Vlugt et al. 2021; Smolčić et al. 2017a); (2) no counterpart is found in the COSMOS2020 catalog (Weaver et al. 2022); and (3) the 1mm flux, $S_{1.1mm} > 3.5$ mJy, using derived fluxes from FIR SED fitting in the Super-deblended catalog (Jin et al. 2018; Jin et al. in prep.). Of the 10 sources, two sources (ID: 600000037, 600000055) were only detected in the deep COSMOS-XS S-band image, while the remaining sources were also detected in the VLA-COSMOS 3GHz catalog (Smolčić et al. 2017a).

Following Dudzevičiūtė et al. (2020), $S_{1.1mm} = 3.5$ mJy corresponds to a 870$\mu$m

Table 5.1. Properties of ALMA-targeted 'optically dark' sources.

| ID | R.A. | Decl. | $S_{3\ \mathrm{GHz}}$ [mJy] | $z_{\mathrm{FIR}}$ [a] |
|---|---|---|---|---|
| 20003080/COSBO-7 | 10h00m23.96s | 2d17m50.03s | 28.6 ± 2.8 | 4.0 ± 0.35 |
| 20004275 | 9h59m35.36s | 2d19m20.14s | 22.3 ± 2.6 | 5.6 ± 0.85 |
| 20004337 | 9h59m21.43s | 2d22m40.07s | 28.4 ± 2.7 | 3.2 ± 0.4 |
| 20004728 | 10h01m35.67s | 2d45m24.81s | 20.4 ± 2.5 | 3.3 ± 0.95 |
| 20004824 | 9h59m01.96s | 2d24m29.25s | 19.9 ± 2.5 | 3.5 ± 0.5 |
| 20005887 | 9h58m53.63s | 2d30m04.57s | 25.0 ± 2.6 | 3.1 ± 0.8 |
| 20006212 | 10h00m54.49s | 2d43m36.21s | 16.2 ± 2.4 | 8.9 ± 2.6 |
| 20007237 | 10h00m00.39s | 2d41m45.17s | 14.7 ± 2.4 | 4.0 ± 1.3 |
| 60000037 | 10h00m05.24s | 2d37m54.18s | 15.3 ± 1.7 | 6.6 ± 2.65 |
| 60000055 | 10h00m24.04s | 2d29m48.55s | 6.4 ± 1.0 | 6.2 ± 2.4 |

**Notes.**

[a] The new Super-deblended FIR-derived redshift and uncertainty based on SED fitting using the procedure from Liu et al. (2018) and Jin et al. (2018).

flux density of 6.3 mJy (adopting $S_{870\mu\mathrm{m}}/S_{1.1\mathrm{mm}} = 1.8$, equivalent to a $\nu \sim 2.5$ spectral index based on the average flux ratio of AS2UDS SMGs from Ikarashi et al. 2017). This is ∼7 times higher than the flux range probed by Smail et al. (2021), who probed NIR-faint SMGs. All targeted sources have a FIR+mm combined detection with $\mathrm{S/N_{FIR}} > 5$, calculated as described in Eq. 2 from Liu et al. (2018). The properties of the selected 'optically dark' sources can be found in Table 5.1. Fig. 5.1 shows the S-band radio observations with contours from the ALMA observations overlaid.

### 5.2.2 ALMA follow-up observations and data reduction

The ALMA Band-3 spectral scans of 10 'optically dark' galaxies were performed at end of January and early March 2023 (project 2022.1.00863.S, PI: Hodge). The observations were centered on the positions with a spectral configuration using three frequency tunings to cover 84-108 GHz with resolution of 7.8 MHz. The spectral configuration is shown in Fig. 5.2 where also can be seen which lines can be detected with this setup. The three separate tunings cover the frequency range with 5 narrow gaps, indicated with the white horizontal lines in Fig. 5.2 and the gray shaded area in the spectra presented in Appendix 5.A. The observations were carried out with the array configuration C4 giving a synthesized beam of 1″. The 10 galaxies were observed in track sharing mode, and each source was observed for 0.5 hr of on-source time in each tuning, reaching typical r.m.s. noise level of 0.12 mJy per 600 km $\mathrm{s^{-1}}$.

The ALMA 3mm data are calibrated and reduced with CASA6.4 (McMullin et al. 2007). We converted the data into uvfits format to perform further analysis with the IRAM GILDAS tool working on the u-v space (visibility) data. The spectra are extracted by fitting models in the u-v space with fixed positions using point source

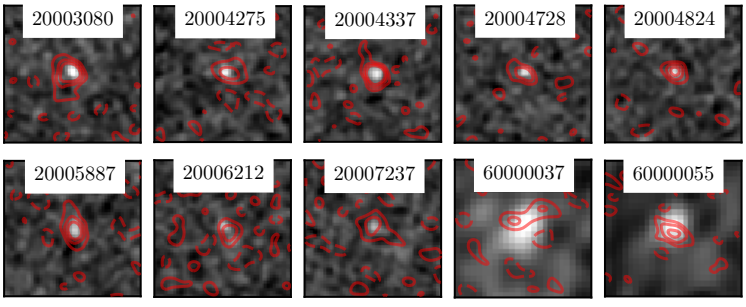


**Figure 5.1:** Radio images of ALMA-targeted 'optically dark' sources with ALMA contours overlaid. Images are $10'' \times 10''$, centered at the centroid of the new Super-deblended catalog entry (Jin et al. in prep.). The gray-scale images are the radio images the S-band VLA-COSMOS 3 GHz Large Project (Smolčić et al. 2017a) and the S-band COSMOS-XS VLA imaging, for 20003080, 20004275, 20004337, 20004728, 20004824, 20005887, 20006212, 20007237 and 60000037 and 60000055, respectively. The red solid contours are the ALMA line imaging for detected CO lines with contours starting at $2\sigma$ and increasing as $4\sigma$ and $6\sigma$. Negative contours at the same significance are shown with red dashed lines. 2000612, 20007237, 60000037 and 60000055 do not show a significant line detection.

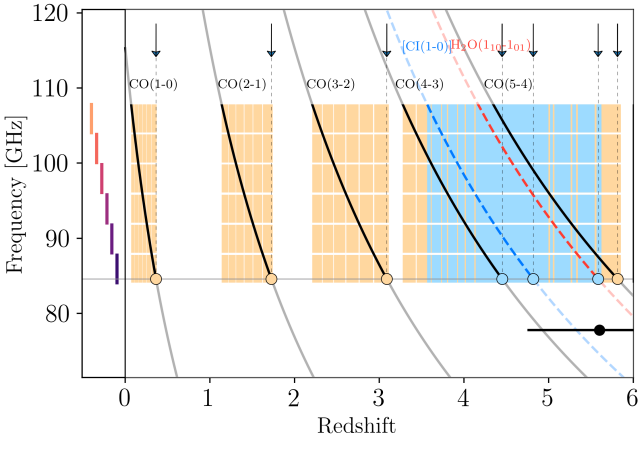


**Figure 5.2:** Graphic showing the full redshift space probed by the frequency coverage of the ALMA spectral scan observations covering 84-108 GHz. This figure was made using the method from Bakx & Dannerbauer (2022). Assuming the observed bandwidths, the filled regions show redshifts where single (orange) and multiple lines ([CI](1-0) in blue and H2O($1_{10}$-$1_{01}$) in red) would be detected for the observed source 20004275. The horizontal line marks the observed line at ∼84.6 GHz, indicating the potential redshift solutions with circles and the top arrows. The black error bar marks the FIR redshift determined for 20004275, see also Table 5.1, using SED fitting.

models. Given that most sources are not detected in 3mm continuum maps, we adopted the radio positions from COMSOS-XS and Smolčić et al. (2017a) catalogs for extracting spectra. We searched iterative for evidence of resolved emission either in the continuum, in the emission-line candidates, and found that only the lensed source 20003080 is resolved and we calibrated for the total line flux using an $3''$ aperture. The spectra with the line detections indicated in green are shown in the figures presented in Appendix 5.A. For sources with two possible redshift solutions, we present the spectrum for each of the solution indicating the different line detections. The velocity averaged maps for the detected CO lines can be seen overlaid on the radio images in Fig. 5.1.

### 5.2.3 Multi-wavelength photometry

The multi-wavelength data used to estimate the 1.1mm flux for the 10 'optically dark' sources are from the latest Super-deblended catalog (Jin et al. in prep.), which adopted the Super-deblending technique (Jin et al. 2018; Liu et al. 2018) by adding priors from the COSMOS-XS sources from the COSMOS-XS catalog (van der Vlugt et al. 2021) and the COSMOS2020 catalog (Weaver et al. 2022). The new Super-deblended catalog in COSMOS (Jin et al. in prep.) has deblended photometry in MIPS 24$\mu$m, *Herschel*, SCUBA-2 450$\mu$m & 850$\mu$m (Wang et al. 2017; Simpson et al. 2019), AzTEC (Aretxaga et al. 2011), MAMBO (Bertoldi et al. 2007), VLA 1.4 & 3 GHz and MeerKAT 1.28 GHz data sets (Schinnerer et al. 2007, 2010; Smolčić et al. 2017a; Jarvis et al. 2016). Fig. 5.3 shows the optical images from the ACS I-band, UltraVISTA $K_S$-band images and IRAC 3.6$\mu$m and 4.5$\mu$m images. All sources have been detected in MIPS, *Herschel*/PACS, at 250$\mu$m, 350$\mu$m and 500$\mu$m, SCUBA-2 and AzTEC. Two sources are also detected in SCUBA-2 at 450$\mu$m. Additionally, three sources have counterparts in IRAC.

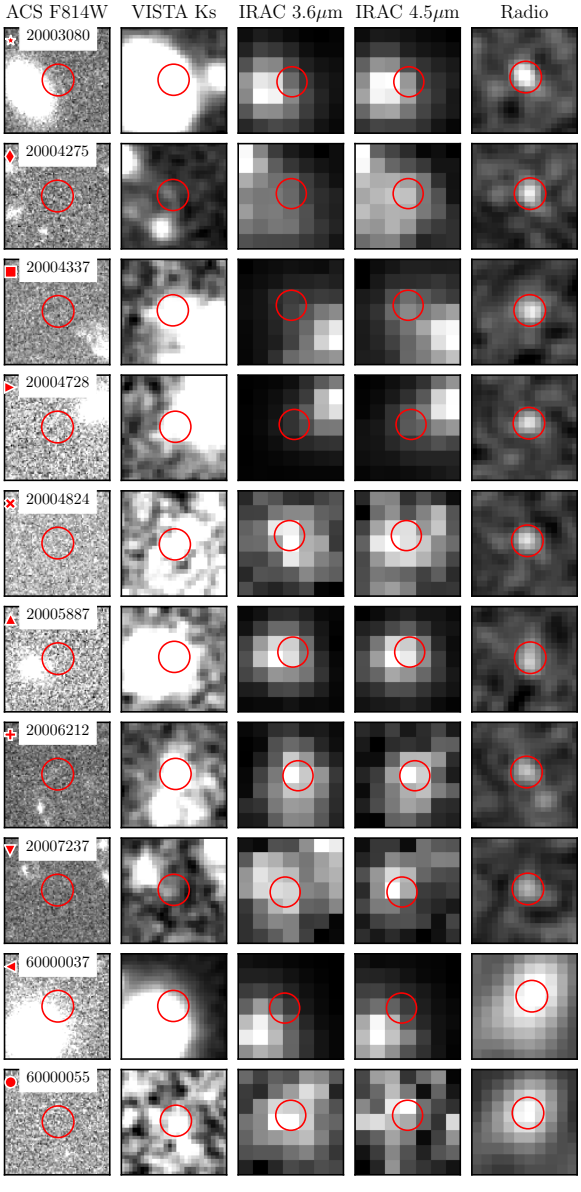


**Figure 5.3:** Postage-stamp images of 10 'optically dark' galaxies targeted with ALMA. From left to right, the optical images from the ACS I-band, UltraVISTA $K_S$-band images and IRAC 3.6$\mu$m and 4.5$\mu$m images and the radio images from the S-band VLA-COSMOS 3 GHz Large Project (Smolčić et al. 2017a) and the S-band COSMOS-XS VLA imaging for 20003080, 20004275, 20004337, 20004728, 20004824, 20005887, 20006212, 20007237 and 60000037 and 60000055, respectively. Each panel has a size of $4'' \times 4''$, centered at the centeroid of the new Super-deblended catalog entry (Jin et al. in prep.). The red circle marks the target galaxies with $0\farcs6$ in radius. The markers next to the source IDs are used throughout the paper to indicate the respective sources.

Table 5.2. Line detections.

| ID | $S/N_{1st}$ [a] | $I_{1st}$ [b] [Jy km $s^{-1}$] | $S/N_{2nd}$ [a] | $I_{2nd}$ [b] [Jy km $s^{-1}$] |
|---|---|---|---|---|
| 20003080 | 11.6 (CO(5-4)) | 1.43 ± 0.20 | ... | ... |
| 20004275 | 4.1 (CO(3-2)) | 0.68 ± 0.26 | ... | ... |
| 20004337 | 14.9 (CO(4-3)) | 1.86 ± 0.31 | ... | ... |
| 20004728 | 8.4 (CO(4-3))/ (CO(5-4)) | 0.45 ± 0.10 | 2.3 ([CI](1-0)) | 0.43 ± 0.24 |
| 20004824 | 6.3 (CO(4-3)) | 0.76 ± 0.18 | 3.6 ([CI](1-0)) | 0.38 ± 0.19 |
| 20005887 | 6.9 (CO(4-3))/ (CO(5-4)) | 0.98 ± 0.40 | 1.4 ($H2O(1_{10}\text{-}1_{01})$) | 0.17 ± 0.20 |
| 20006212[c] | 4.6 (CO(5-4)) | 0.93 ± 0.40 | ... | ... |
| 20007237 | 2.9 (CO(4-3))/ (CO(5-4)) | 0.49 ± 0.18 | 2.6 ([CI](1-0)) | 0.46 ± 0.26 |
| 60000037 | 3.3 (CO(3-2))/ (CO(4-3)) | 0.33 ± 0.12 | 1.1 ($H2O(1_{10}\text{-}1_{01})$) | 0.11 ± 0.15 |
| 60000055[d] | 4.0 (CO(5-4)) | 0.49 ± 0.18 | 1.4 ([CI](1-0)) | 0.12 ± 0.2 |

**Notes.**

[a] Signal-to-noise ratio of the 1st/2nd line.

[b] Flux density of the 1st/2nd line.

[c] This line is confirmed by a [CII] 158$\mu$m detection in ALMA archival data (ID: 2021.1.00280.L, PI: R. Herrera-Camus).

[d] This line is confirmed by the recent observations from Sillaseen et al. (in prep.).

## 5.3 Properties of the galaxies

### 5.3.1 Line identification

To search for emission line features in the observed ALMA 3mm blind line scans, we follow the technique described by Jin et al. (2019). We search for the single emission-line feature with the highest signal-to-noise ratio for each galaxy, following the same line-searching algorithm applied in Daddi et al. (2015), Coogan et al. (2018), and Puglisi et al. (2019). The found lines are then fitted with a Gaussian profile and the Gaussian fits are shown in the figures presented in Appendix 5.C. The flux of the lines is found by integrating over the full width at zero intensity (FWZI) range (e.g., Emonts et al. 2014; Coogan et al. 2018; Jin et al. 2019). The signal-to-noise ratio is given by the weighted mean of the channels over the FWZI range. The signal-to-noise ratio and flux density are given in Table 5.2.

After a detection of a line which we assume to be CO, we searched for additional matching lines: [CI](1-0) or $H2O(1_{10}\text{-}1_{01})$. We know that the secondary lines are typically fainter than CO lines (e.g., Walter et al. 2011; Yang et al. 2019). We use the redshift solutions and velocity range as determined by the primary line. A tentative second line is detected for two sources with one redshift solution: 20004824 and 60000055. A tentative second line is detected for all sources with two redshift solutions: 20004728, 20005887, 20007237 and 60000037. The spectra with the line detections indicated in green are shown in the figures presented in Appendix 5.A. For

sources with two redshift solutions two spectra are given for both redshift solutions indicating all possible line detections.

In six sources we are able to determine the redshift unambiguously with the observed line transitions. The line detections are shortly summarized below and the spectra can be found in Appendix 5.A. First we will discuss 20003080/COSBO-7. The source was originally selected from the IRAM MAMBO 1.2mm survey by Bertoldi et al. (2007) and identified as a lensing system by (Jin et al. 2018), in which the high-z sub-mm galaxy is lensed by a foreground elliptical galaxy at $z_{\rm spec} = 0.36$ by a factor of 3.6 (Jin et al. in prep.). In 20003080/COSBO-7 we observe a strong CO line at ∼95.4 GHz. Since we do not detect [CI](1-0) at ∼102 GHz, which is inconsistent with [CI](1-0)/CO(4-3) numbers in the literature (Bothwell et al. 2017; Jin et al. 2022), we are able to determine this is the CO(5-4) line and the source lies at $z = 5.042$. The ortho-H2O($1_{10}$-$1_{01}$) is not detected, because (1) it is on the edge of spectral window; and (2) this line is expected to be absorbed by the cosmic background at $z = 5$ from the models in Riechers et al. (2013). A detailed study of COSBO-7 with JWST data will be carried out by Jin et al. (in prep.). For 20004275, we detect just one line at the low end of the spectrum at ∼84.6 GHz. The only line we are able to detect at this end of the spectrum which also matches the photometric redshift best is CO(3-2) as is shown in Fig. 5.2. The redshift of this source is thus determined to be $z = 3.087$. Similarly, for 20004337, we detect just one line at the high end of the spectrum at ∼107.5 GHz. The only single line we are able to detect at this end of the spectrum is CO(4-3) and the redshift of this source is thus determined to be $z = 3.285$. One line detection and one tentative line detection with S/N = 3.6 are determined for 20004824 at ∼93 GHz and ∼99.5 GHz, respectively. The only two lines that can be observed this close are CO(4-3) and [CI](1-0). The redshift of this source is thus determined to be $z = 3.955$. In 20006212 we detect one line close to the gap in the frequency coverage. However, we are able to determine the redshift to be $z = 4.539$ since it has [CII] 158$\mu$m detection in ALMA archival data (ID: 2021.1.00280.L, PI: R. Herrera-Camus). The detected line thus corresponds to CO(5-4). For 60000055 we are able to, with the addition of the recent observations from Sillaseen et al. in prep., detect a line at ∼99 GHz. With the tentative detection of [CI](1-0) at ∼84.5 GHz, we are able to determine the redshift for 60000055 at $z = 4.820$.

For four sources with line transitions, we find two redshift solutions. In 20004728 we find a tentative line with S/N = 2.3 close to the gap in the frequency coverage at ∼88 GHz. In addition, we detect a significant line at ∼103 GHz. Because the line close to the frequency gap is only a tentative detection, the line detected at ∼103 GHz can be CO(4-3) or CO(5-4). The redshift for 20004728 can thus be either $z = 3.485$ or $z = 4.606$. For 20005887, we find one CO line at ∼93.5 GHz. In addition, we find one tentative line with S/N = 1.4 at ∼91.5 GHz which could be H2O($1_{10}$-$1_{01}$) if the CO transition corresponds to CO(5-4). The [CI](1-0) line that would be observed if the CO transition corresponds to CO(4-3) lies close to the frequency gap at ∼93 GHz and can thus not be detected. Because of the frequency gap and the tentative line detection, we can not find a single redshift solution. The redshift for 20005887 can thus be either $z = 3.934$ or $z = 5.167$. For 20007237, we find one tentative CO line with S/N = 2.9 at ∼98 GHz. The [CI](1-0) line that would be observed if the CO transition corresponds to CO(5-4) lies close to the low end of the frequency range at

∼84 GHz and can thus not be detected. In addition, we find one tentative line at ∼104.5 GHz with S/N = 2.6 which could be [CI](1-0) if the CO transition corresponds to CO(4-3). Because of the frequency range and the tentative line detection, we can not find one redshift solution. The redshift solutions for 20007237 that also match the photometric redshift ($z_{\rm FIR} = 4.0 \pm 1.3$) can be either $z = 3.7$ if the tentative CO transition corresponds to CO(4-3) or $z = 4.868$ if the tentative CO transition corresponds to CO(5-4). Lastly, for 60000037, we do not detect any significant CO line, the signal-to-noise ratio of the line at ∼86.8 GHz is S/N = 3.3. In addition, we can find one tentative line with S/N = 1.1 at ∼105 GHz if the CO transition corresponds to CO(4-3) which could be H2O($1_{10}$-$1_{01}$). We therefore have two redshift solutions with $z = 2.08$ and $z = 4.3$.

The sky density of the 8 ALMA-confirmed 'optically dark' sources with $S_{1.1\rm mm} > 3.5\,$mJy and a line detection is $16.7 \pm 5.9\,{\rm deg}^{-2}$. As expected this sky density is lower than the potential surface density found by Smail et al. (2021) of $450^{+750}_{-300}\,{\rm deg}^{-2}$ for NIR-faint SMGs with $S_{870\mu\rm m} \geq 1\,$mJy which is equivalent to $S_{1\rm mm} \geq 0.56\,$mJy. Smail et al. (2021) thus probe a flux range ∼7 times lower than the range probed by this study as discussed in Section 5.2.1. Three sources from the sub-sample discussed by Smail et al. (2021) have $S_{870\mu\rm m} \geq 6.3\,$mJy in the AS2UDS catalog (Stach et al. 2019) and would thus be selected from the 0.96 deg$^2$ field with the flux cut of $S_{1.1\rm mm} > 3.5\,$mJy. This gives a sky density of $3.125 \pm 1.8\,{\rm deg}^{-2}$, significantly below the sky density found in this study. Similarly, our sky density is also significantly lower than the ALMA-selected $H$–dropout surface density corrected for incompleteness of $530\,{\rm deg}^{-2}$ (Wang et al. 2019) with $S_{870\mu\rm m} \geq 0.6\,$mJy which is equivalent to $S_{1\rm mm} \geq 0.33\,$mJy.

### 5.3.2 Redshifts

For the 10 sources in the sample, the median redshift, including the low-$z$ solutions for the sources with two redshift solutions, is $z = 3.82$, with a 16-84th percentile range of $z = (3.2 - 4.7)$. The median redshift, including the high redshift for the sources with two redshift solutions, is $z = 4.57$, with a 16-84th percentile range of $z = (3.6 - 5.0)$. 7/10 sources agree with their found spectroscopic redshift to their estimated FIR photometric redshift within $<2\sigma$. Hence the spectroscopic redshifts confirm that all of the 'optically dark' sources targeted are at $z \gtrsim 3$ as suggested by their estimated FIR photometric redshifts. The estimated redshifts are presented in Table 5.3. The comparison between the FIR-based photometric redshifts and the redshifts derived using ALMA 3mm line scans are shown in Fig. 5.4.

### 5.3.3 SED fitting

We collected the new Super-deblended FIR/(sub-)millimeter photometry together with the ALMA 3mm continuum measurements and redshifts as determined above to fit the full SEDs. For the four sources for which we find two redshift solutions, we fit for both of the solutions. In the SED fitting four distinct SED components are used: (1) a stellar component (Bruzual & Charlot 2003) with a Small Magellanic Cloud dust attenuation law (indicated in blue); (2) a mid-infrared AGN torus component (Mul-

Table 5.3. Derived properties of 'optically dark' sources.

| ID | $z_{\rm ALMA}$[a] | $\rm SFR_{FIR}$ $[\rm M_\odot\ yr^{-1}]$ | $L_{\rm IR}$ $[10^{12}\ L_\odot]$ |
|---|---|---|---|
| 20003080[b] | 5.041 | 220.2 ± 64.4 | 2.2 ± 0.6 |
| 20004275 | 3.087 | 412.2 ± 3.6 | 4.1 ± 0.04 |
| 20004337 | 3.285 | 701.7 ± 4.3 | 7.0 ± 0.04 |
| 20004728 | **3.485**/4.606 | **579.6 ± 58.5**/1187.8 ± 62.4 | **5.8 ± 0.6**/11.9 ± 0.6 |
| 20004824 | 3.955 | 789.3 ± 175.6 | 7.9 ± 1.8 |
| 20005887 | **3.943**/5.167 | **804.2 ± 159.1**/1583.0 ± 52.2 | **8.0 ± 1.6**/15.8 ± 0.5 |
| 20006212 | 4.539 | 617.9 ± 318.7 | 6.2 ± 3.2 |
| 20007237 | **3.7**/4.868 | **481.9 ± 4.5**/995.4 ± 145.1 | **4.8 ± 0.04**/10.0 ± 1.5 |
| 60000037 | 2.98/**4.3** | 253.2 ± 2.0/**487.4 ± 87.1** | 2.5 ± 0.02/**4.9 ± 0.9** |
| 60000055 | 4.82 | 358.4 ± 6.0 | 3.6 ± 0.06 |

**Notes.**

[a] The 'best' redshift solutions for sources with two redshift solutions as determined in Section 5.3.4 are indicated in bold.

[b] 20003080 is lensed by a factor of 3.6 (Jin et al. in prep.), therefore the physical parameters noted here are divided by 3.6.

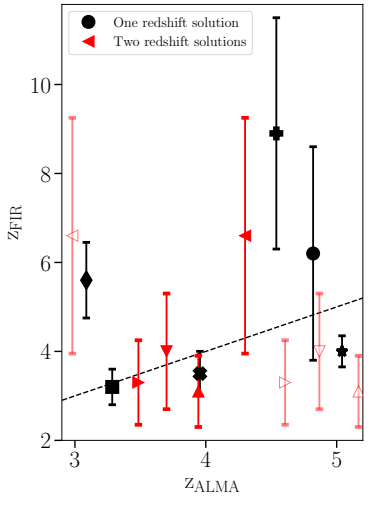


**Figure 5.4:** Comparison between the FIR-based photometric redshifts from the new Super-deblended catalog (Jin et al. in prep.) and the redshifts derived using ALMA 3mm line scans. Black and red symbols indicate sources with one and two redshift solutions, respectively. The markers refer to individual sources as shown in Fig. 5.3. Closed red symbols indicate the 'best' redshift solutions for sources with two redshift solutions as determined in Section 5.3.4.

laney et al. 2011, indicated in red); (3) dust continuum emission (indicated in green) from the Magdis et al. (2012) library with the more updated $L_{\rm IR}/{\rm M}_{\rm dust}$-redshift evolution taken from Béthermin et al. (2015); and (4) a power-law radio continuum with an evolving radio-FIR correlation ($q_{\rm TIR}$). Extra details on the SED fitting procedure can be found in Liu et al. (2018) and Jin et al. (2018). The results for the fitted SEDs for the 10 sources can be found in Appendix 5.B.

### 5.3.4 Far-infrared luminosity

Using the derived SEDs, the IR luminosities ($L_{\rm IR}$) are taken as the pure dust component $L_{\rm IR}$ over 8–1000$\mu$m, excluding any AGN torus components. For the sample, the median FIR luminosity, including the low redshift solutions for the sources with two redshift solutions, is $L_{\rm IR} = (5.3 \pm 0.3) \times 10^{12} L_{\odot}$, with a 16-84th percentile range of $L_{\rm IR} = (3.8 - 7.9) \times 10^{12} L_{\odot}$. The median FIR luminosity, including the high redshift solutions for the sources with two redshift solutions, is $L_{\rm IR} = (6.6 \pm 0.6) \times 10^{12} L_{\odot}$, with a 16-84th percentile range of $L_{\rm IR} = (4.5 - 11.0) \times 10^{12} L_{\odot}$. 8 sources from the sample are classified as ULIRGs with $L_{\rm IR} = 1 - 10 \times 10^{12} L_{\odot}$. None of the sources are LIRGs with $L_{\rm IR} < 1 \times 10^{12} L_{\odot}$ and 2 sources can be determined to be HyLIRGs with $L_{\rm IR} > 1 \times 10^{13} L_{\odot}$ assuming their highest redshift solution lying at $z \sim 4.6$ and $z \sim 5.2$. Local ULIRGs have considerably lower FIR luminosities as derived by Dudzevičiūtė et al. (2020) for the GAMA local ULIRG sample (Driver et al. 2018) with a median of $L_{\rm IR} = (1.41 \pm 0.03) \times 10^{12} L_{\odot}$ and a 16-84th percentile range of $L_{\rm IR} = (1.1 - 2.4) \times 10^{12} L_{\odot}$. We can thus conclude that the observed sample is comparable to SMGs as they have some FIR luminosities higher or similar to local ULIRGs. In addition, we find that the redshifts of these sources form the high-redshift tail as all observed sources have a redshift $z \gtrsim 3$ (Simpson et al. 2014). The FIR luminosities determined for the sample are somewhat higher than the median FIR luminosity of the 1.1mm selected SMG sample from Miettinen et al. (2017), who derive a median of $L_{\rm IR} = (4.0 \pm 0.3) \times 10^{12} L_{\odot}$ for a sample with an flux density range of 0.83-11.1 mJy which is close to the selection criterion of $S_{1.1{\rm mm}} > 3.5\,{\rm mJy}$. The median FIR luminosity determined in this study is also higher compared to the FIR luminosities Dudzevičiūtė et al. (2020) derived for their sample of 707 SMGs with flux densities in the range $S_{870\mu{\rm m}} = 0.6 - 13.6$ mJy. They find a median FIR luminosity of $L_{\rm IR} = (2.88 \pm 0.09) \times 10^{12} L_{\odot}$.

#### Correlation between $L'_{\rm CO(5\text{-}4)}$ and $L_{\rm IR}$

The CO(5-4) transition is believed to be a good tracer of the star-forming gas, resulting in an almost linear $L'_{\rm CO(5\text{-}4)}$–$L_{\rm IR}$ correlation. Daddi et al. (2015) find that this linear correlation between $L_{\rm CO(5\text{-}4)}$ and $L_{\rm IR}$ can be described by $\log L'_{\rm CO(5\text{-}4)} = \log L_{\rm IR}/L_{\odot} - 2.52$ with a dispersion of 0.24 dex, which is remarkable for a relation spanning 4 orders of magnitude along either axes. In addition, it holds for normal and starburst galaxies both locally and at high redshift. It is thus interesting to verify where the sources that have a detected CO(5-4) line lie on the $L'_{\rm CO(5\text{-}4)}$ and $L_{\rm IR}$ plane. In addition, we can use this relation to check whether the CO transitions detected in 20004728, 20005887, 20007237 and 60000037 correspond to CO(5-4), CO(4-3) or

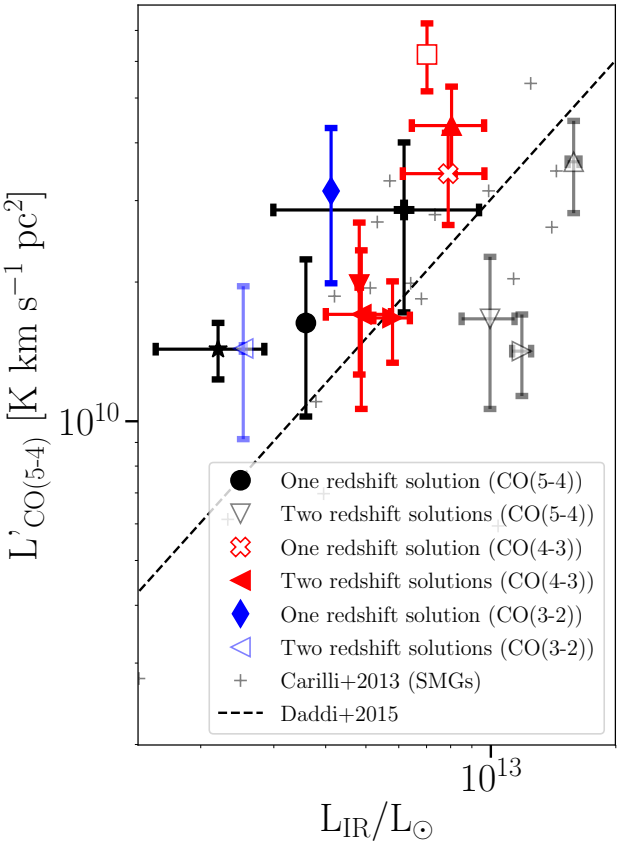


**Figure 5.5:** The CO(5-4) line luminosity versus the IR luminosity. All sources with a detected CO(5-4) line are indicated with black closed symbols. Sources with a possible CO(5-4) line detection are indicated with black open symbols. The sources with an extrapolated CO(5-4) line luminosity from the measured CO(4-3) line luminosity are indicated with the red closed and open symbols; the open symbols indicate an detected CO(4-3) line and the closed symbols indicate a possible CO(4-3) line detection. The sources with an extrapolated CO(5-4) line luminosity from the measured CO(3-2) line luminosity are indicated with blue symbols; the open symbol for the source with a possible CO(3-2) line detection and the closed symbol for the source with an detected CO(3-2) line detection. The markers refer to individual sources as shown in Fig. 5.3. The dotted line gives the correlation between the CO(5-4) line luminosity with the IR luminosity from Daddi et al. (2015). Crosses indicate literature SMGs from Carilli & Walter (2013).

CO(3-2). When the calculated luminosities ($L'_{\mathrm{CO(5\text{-}4)}}$) lie on the linear correlation, they are likely to originate from the CO(5-4) transition.

To obtain the integrated line flux $S_{\mathrm{CO(5\text{-}4)}}$, we fit the lines indicated in green in the 1D spectrum, shown in the figures presented in Appendix 5.A, with a Gaussian profile and integrate over the FWZI range. The fitting results can be found in Appendix 5.C. From the line flux we can then determine the luminosity as defined in Solomon et al. (1992):

$$L'_{\mathrm{CO(5\text{-}4)}} = 3.25 \times 10^7 \frac{S_{\mathrm{CO(5\text{-}4)}} D_{\mathrm{L}}^2}{(1+z)^3 \nu_{\mathrm{obs}}^2}\,, \tag{5.1}$$

where the CO line luminosity, $L'_{\mathrm{CO(5\text{-}4)}}$, is measured in K km s$^{-1}$pc$^2$; $S_{\mathrm{CO(5\text{-}4)}}$ is the CO integrated flux density in units of Jy km s$^{-1}$, $D_{\mathrm{L}}$ to the luminosity distance at redshift $z$, in Mpc, and $\nu_{\mathrm{obs}}$ is the observing frequency in GHz. Fig. 5.5 shows the correlation of the CO(5-4) line luminosity with the IR luminosity of all the sources with a detected CO(5-4) line (20003080, 20006212 and 60000055) and the sources with a possible CO(5-4) line detection (20004728, 20005887 and 20007237) together with the best-fitting relations from Daddi et al. (2015). In addition, we compare the sources to $L'_{\mathrm{CO(5\text{-}4)}}$–$\mathrm{L_{IR}}$ of SMGs taken from the compilation of Carilli & Walter (2013). In addition, Fig. 5.5 shows the correlation of the CO(5-4) line luminosity with the IR luminosity of all the sources with a detected CO(4-3) line (20004337 and 20004824) and the sources with a possible CO(4-3) line detection (20004728, 20005887, 20007237 and 60000037). The CO(5-4) luminosities shown in Fig. 5.5 for these sources are extrapolated as $1.67 \times L'_{\mathrm{CO(4\text{-}3)}}$ (assuming $\mathrm{r_{54/10}} = 0.7$ and $\mathrm{r_{43/10}} = 0.6$; Stanley et al. 2023). Fig. 5.5 also shows the correlation of the CO(5-4) line luminosity with the IR luminosity of the source with a detected CO(3-2) line (20004275) and the source with a possible CO(3-2) line detection (60000037). The CO(5-4) luminosities shown in Fig. 5.5 for these sources are extrapolated as $1.0 \times L'_{\mathrm{CO(3\text{-}2)}}$ (assuming $\mathrm{r_{54/10}} = 0.7$ and $\mathrm{r_{32/10}} = 0.7$; Stanley et al. 2023).

We find all sources fall within the range expected for SMGs. First we will discuss the six sources with a confirmed redshift. We have to note that the line for 20006212 is detected close to the gap in the frequency coverage. Therefore, we only measure about half of the line luminosity and have to extrapolate beyond the gap. This source and 60000055 lie within $0.9\sigma$ of the $L'_{\mathrm{CO(5\text{-}4)}}$–$\mathrm{L_{IR}}$ correlation from Daddi et al. (2015) whereas 20003080 lies within $3.9\sigma$. For the two sources with an extrapolated $L'_{\mathrm{CO(4\text{-}3)}}$, 20004337 and 20004824, we find they lie within $4.0\sigma$ and $1.3\sigma$, respectively.

For the source with an extrapolated $L'_{\mathrm{CO(3\text{-}2)}}$ (20004275) we find it lies within $1.6\sigma$. Next, we will discuss the four sources with two redshift solutions. For 20004728, 20005887 and 20007237 we find they lie within, respectively, $7.5\sigma$, $1.4\sigma$ and $2.2\sigma$ of the correlation assuming a CO(5-4) line. They lie within, respectively, $0.2\sigma$, $2.0\sigma$ and $0.7\sigma$ assuming a CO(4-3) line. For 60000037 we find it lies within $0.4\sigma$ and $1.3\sigma$ assuming a CO(4-3) line and a CO(3-2) line, respectively.

From this analysis, we find that 20004728, 20007237 and 60000037 are most likely to have a CO(4-3) detection implying that these sources would lie at, respectively, $z = 3.5$, $z = 3.7$ and $z = 4.3$. This is also in line with the redshifts derived from SED-fitting shown in Fig. 5.4. For 20005887, the difference between assuming a CO(5-4) line and assuming a CO(4-3) line is only $0.6\sigma$. Since the redshift derived from SED-

fitting ($z_{\rm FIR} = 3.1 \pm 0.8$) lies closest to the redshift found when assuming the detected line corresponds to CO(4-3) ($z_{\rm ALMA} = 3.9$), we find that this sources is most likely to have a CO(4-3) detection. We thus determine a 'best' redshift for each source, which is indicated in bold in Table 5.3. Assuming these redshifts, the median redshift of the 10 sources is then $z = 3.95 \pm 0.62$, with a 16-84th percentile range of $z = (3.4 - 4.7)$. The median $L_{\rm IR}$ assuming these redshifts is $L_{\rm IR} = (5.3 \pm 0.6) \times 10^{12} L_{\odot}$, with a 16-84th percentile range of $L_{\rm IR} = (3.8 - 7.5) \times 10^{12} L_{\odot}$. In the following sections and figures, we will continue to show both solutions since the above test only indicates which redshift would be 'better' but does not constrain the redshift with certainty.

### 5.3.5 Star formation rates

The IR luminosity traces dust-obscured star formation, assuming a Chabrier IMF (Chabrier 2003) and the relation SFR $= L_{\rm IR}/(1 \times 10^{10}\, L_{\odot})\, {\rm M_{\odot} yr^{-1}}$ (Daddi et al. 2010) we determine a median SFR, including the low redshift solutions for the sources with two redshift solutions, of SFR $= 530.8 \pm 32.2\, {\rm M_{\odot} yr^{-1}}$ with a 16-84th percentile range of SFR $= 299.5 - 750.8\, {\rm M_{\odot} yr^{-1}}$. The median SFR, including the high redshift solutions for the sources with two redshift solutions, is SFR $= 659.8 \pm 63.4\, {\rm M_{\odot} yr^{-1}}$ with a 16-84th percentile range of SFR $= 382.1 - 1103.1\, {\rm M_{\odot} yr^{-1}}$. The estimated SFRs are presented in Table 5.3. Assuming the 'best' redshifts, as determined in Section 5.3.4, we find a median SFR of SFR $= 533.5 \pm 61.5\, {\rm M_{\odot} yr^{-1}}$ with a 16-84th percentile range of SFR $= 382.1 - 750.8\, {\rm M_{\odot} yr^{-1}}$.

Since we also have radio detections for all of the observed sources, we are able to compare the SFR calculated from the IR luminosity to the SFR that can be derived from the radio luminosity. Rest-frame 1.4 GHz luminosities are determined using the measured spectral index for the required K-corrections if available. When only a single radio flux is available, a spectral index of $\alpha = -0.7$ is assumed instead. The luminosities are then calculated through

$$L_{1.4\,\rm GHz} = \frac{4\pi D_L^2}{(1+z)^{1+\alpha}} S_{1.4\,\rm GHz}\,. \tag{5.2}$$

Here $D_L$ is the luminosity distance to redshift $z$ and $S_{1.4\ \rm GHz}$ is the observed flux density at 1.4 GHz. Having the rest-frame 1.4 GHz luminosities, we are now able to estimate the SFRs from radio luminosities. To convert luminosity into a SFR, we follow van der Vlugt et al. (2022):

$${\rm SFR}(L_{1.4\,\rm GHz}) = f_{\rm IMF}\, 10^{-24}\, 10^{q_{\rm TIR}(z)}\, L_{1.4\,\rm GHz}\,, \tag{5.3}$$

where SFR is the SFR in units of ${\rm M_{\odot} yr^{-1}}$, $f_{\rm IMF}$ is a factor accounting for the IMF ($f_{\rm IMF} = 1$ for a Chabrier IMF and $f_{\rm IMF} = 1.7$ for a Salpeter IMF) and $L_{1.4\,\rm GHz}$ is the rest-frame 1.4 GHz luminosity in units of W ${\rm Hz^{-1}}$. For $q_{\rm TIR}$ we use the radio-FIR correlation found by Delvecchio et al. (2021):

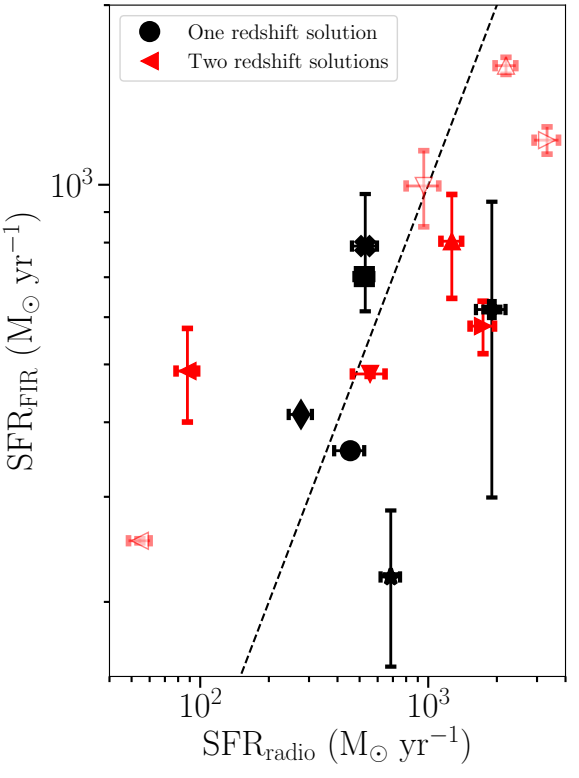


**Figure 5.6:** Comparison between the star formation rate determined from the infrared luminosity derived by SED fitting and the star formation rate derived from radio luminosity. The dotted line describes the one-to-one relation. Black and red symbols indicate sources with, respectively, one and two redshift solutions. The markers refer to individual sources as shown in Fig. 5.3. Closed red symbols indicate the 'best' redshift solutions for sources with two redshift solutions as determined in Section 5.3.4.

$$q_{\mathrm{TIR}}(\mathrm{M}_\star, z) = 2.646 \times (1+z)^{-0.023} - 0.148 \times (\log_{10} \frac{\mathrm{M}_\star}{\mathrm{M}_\odot} - 10)\,. \quad (5.4)$$

For the mass ($M_\star$), we assume the same mass for every source of $M_\star = 2.8 \times 10^{10} M_\odot$ which was the mass for 'optically dark'/faint galaxies derived by Xiao et al. (2023) from SED fitting with median stacked photometry.

For two sources we find their radio SFR is ∼3 times higher than what was expected based on the FIR luminosity: 20003080 and 20006212. 20004728 also has a high radio SFR for both redshift solutions, the radio SFR is 3.0 times and 2.8 times higher

than what was expected based on the FIR luminosity. This is likely due to AGN contamination which increases the radio luminosity. Accreting supermassive black holes (SMBHs) in AGN can also accelerate the electrons that produce synchrotron emission. This AGN contribution would also result in a strong deviation from the FIR-radio correlation expected for star-forming sources. This will be discussed in the next section. We do find one outlier located far above the one-to-one line in both redshift solutions at the low end of radio SFR: 60000037. This is a source for which we did not measure a significant line. This shows that the inferred FIR luminosity might be overestimated in the current SED-fit based on the current redshift solutions. It also shows the importance of having spectroscopic redshifts for SED-fitting.

### 5.3.6 Radio-FIR correlation

Attempts have been made to study the radio-FIR correlation in high-z SMGs at $z > 3$ (e.g., Miettinen et al. 2017; Algera et al. 2020b). These studies found that these sources generally lie significantly below the canonical $q_{\rm TIR}$ ratio of local normal SFGs. Miettinen et al. (2017) studied the physical properties of 16 SMGs in the redshift range of $z = 1.6 - 5.3$ in the COSMOS field. They found a median of $q_{\rm TIR} = 2.27^{+0.27}_{-0.13}$, shown as the green shaded region in Fig. 5.7, using the radio luminosity derived from 325 MHz and the IR luminosity derived with MAGPHYS. A similar value was found by Algera et al. (2020b). They measured the $q_{\rm TIR}$ of 273 SMGs with 1.4 GHz detections, and found a median $q_{\rm TIR} = 2.20 \pm 0.03$ independent of redshift, shown as the blue shaded region in Fig. 5.7. We find that the measured $q_{\rm TIR}$ values are broadly in line with Miettinen et al. (2017) and Algera et al. (2020b). Assuming the 'best' redshifts, we find a median $q_{\rm TIR}$ of $q_{\rm TIR} = 2.41 \pm 0.08$ with a 16-84th percentile range of $q_{\rm TIR} = 2.01 - 2.67$. The $q_{\rm TIR}$ values fall generally close and below the values found for local, typically less strongly star-forming galaxies with an average $q_{\rm TIR} = 2.64 \pm 0.02$ (Bell 2003) and local ULIRGs with an average $q_{\rm TIR} = 2.7 \pm 0.06$ (Farrah et al. 2003), indicated with the dashed line in Fig. 5.7. We do find one outlier located far above the $q_{\rm TIR}$ found by Farrah et al. (2003) in both redshift solutions: 60000037. This is a source for which we did not detect a significant line. Since such values are unexpected for SMGs and rare for high redshift radio selected sources (Delvecchio et al. 2021), this shows that the inferred FIR luminosity and following from that $q_{\rm TIR}$ might be overestimated in the current SED-fit. 20003080, 20006212 and 20004728 can be found at the low end of the radio-FIR correlation as we expected based on their radio SFR. However we do not find a significant deviation from the $q_{\rm TIR}$ found by Algera et al. (2020b). If AGN contamination is the cause of the deviation, it is only a small contribution as expected for SMGs. In conclusion, both IR and radio can be used to trace the SFR for dust-obscured star formation. In addition, the $q_{\rm TIR}$ found for these sources are below the local correlation for both normal star-forming galaxies and local ULIRGs.

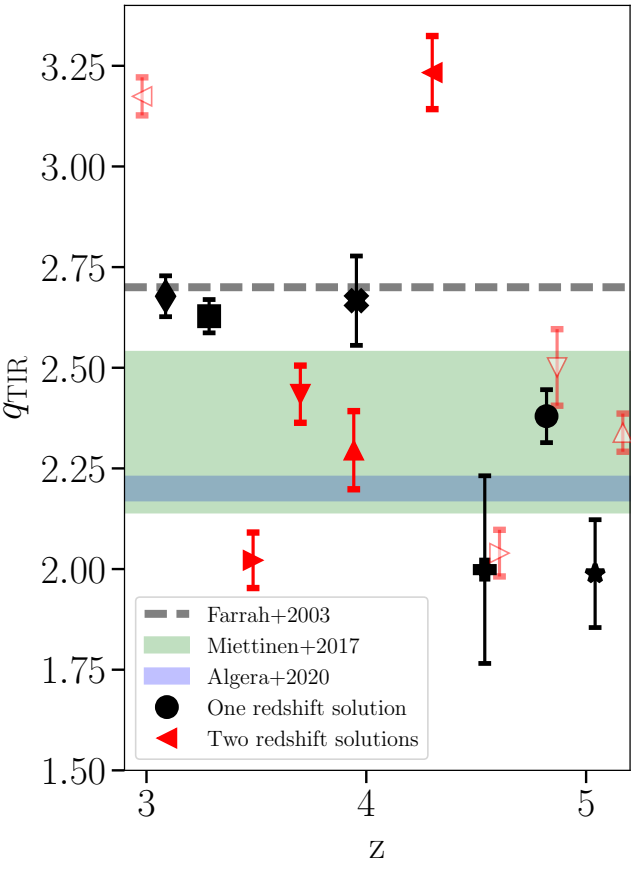


**Figure 5.7:** The $q_{\rm TIR}$ values for the 10 'optically dark' sources compared to the $q_{\rm TIR}$ for 16 SMGs in the COSMOS field (Miettinen et al. 2017), a sample of radio-detected SMGs from the AS2UDS survey (Algera et al. 2020b) and local ULIRGs (Farrah et al. 2003). Black and red symbols indicate sources with, respectively, one and two redshift solutions. The markers refer to individual sources as shown in Fig. 5.3. Closed red symbols indicate the 'best' redshift solutions for sources with two redshift solutions as determined in Section 5.3.4.

## 5.4 Contribution to the cosmic star formation rate density history

The SFRD is the star formation in galaxies over a given co-moving volume. To estimate the contribution and importance of the $S_{1.1\mathrm{mm}} > 3.5\,\mathrm{mJy}$ selected 'optically dark' sources, we calculate their SFRD and compare it to literature data. As the 'optically dark' sources were discovered within a radio survey area, we can simply calculate their SFRD by using their total SFR divided by the survey volume. We will use the SFR estimated from the FIR based SED. Since this SFR estimate is derived from a dust component excluding AGN torus components in contrast to the radio SFR which might be contaminated by some contribution from the AGN as discussed in Section 5.3.5. In addition, the FIR-derived SFR should be a good estimate of the total SFR as we expect a low $\mathrm{SFR_{UV}}$ contribution. Franco et al. (2020) found the $\mathrm{SFR_{UV}}$ contributes only 1% to the total SFR in the 35 galaxies detected at 1mm in the GOODS-ALMA field.

To calculate the SFRD, we need the survey volume. This is the volume between the shells defined by the redshift range of the sources, within a solid angle:

$$\begin{aligned} V &= \frac{\Omega}{4\pi}(V_{z_1} - V_{z_0})\,; \\ &= \frac{\Omega}{4\pi}[\frac{4\pi}{3}(d_{z_1}^3 - d_{z_0}^3)]\,; \\ &= \frac{\Omega}{3}[(d_{z_1}^3 - d_{z_0}^3)]\,, \end{aligned} \tag{5.5}$$

where the solid angle $\Omega$ corresponds to the effective area of the L-band observations: $0.48\,\mathrm{deg}^2$, in units of steradian $1.45 \times 10^{-4}$ sr; and $d_{z_0}$ and $d_{z_1}$ correspond to the co-moving distances at given redshifts of $z_0$ and $z_1$ (Shu et al. 2022; Xiao et al. 2023). Since the sample size is limited, we consider a single redshift bin with a broad redshift range in which all detected sources are included.

The cosmic SFRD for the total sample is:

$$\mathrm{SFRD} = \frac{\sum_i \mathrm{SFR}_i}{V}\,, \tag{5.6}$$

where the $\mathrm{SFR}_i$ is the FIR-based SFR given for each galaxy. The SFRD of the 10 sources, assuming the highest redshift for sources with two redshift solutions, reaches approximately $6.92 \pm 0.39 \times 10^{-4}\,\mathrm{M_\odot yr^{-1}Mpc^{-3}}$ with the mean redshift of $z_{\mathrm{mean}} = 4.37$ (and $z_{\mathrm{median}} = 4.57$). The SFRD of the 10 sources, assuming the lowest redshift for sources with two redshift solutions, reaches approximately $3.90 \pm 0.38 \times 10^{-4}\,\mathrm{M_\odot yr^{-1}Mpc^{-3}}$ with the mean redshift of $z_{\mathrm{mean}} = 3.88$ (and $z_{\mathrm{median}} = 3.82$). The SFRD of the 10 sources, assuming the 'best' redshift for sources with two redshift solutions, reaches approximately $5.42 \pm 0.41 \times 10^{-4}\,\mathrm{M_\odot yr^{-1}Mpc^{-3}}$ with the mean redshift of $z_{\mathrm{mean}} = 4.02$ (and $z_{\mathrm{median}} = 3.95$).

Fig. 5.8 shows the SFRD derived from $S_{1.1\mathrm{mm}} > 3.5\,\mathrm{mJy}$ selected 'optically dark' sources. In addition, Fig. 5.8(a) shows a variety of observational studies (Wang et al.

2019; Dudzevičiūtė et al. 2020; Gruppioni et al. 2020; Talia et al. 2021; Enia et al. 2022; Shu et al. 2022; Barrufet et al. 2023; Xiao et al. 2023) determining the contribution of 'optically dark' sources. The observations span a wide range of SFRD values over an order of magnitude at $3 \lesssim z \lesssim 6$. A further discussion on the differences of these studies can be found in van der Vlugt et al. (2023). Assuming the 'best' redshifts for sources with two redshift solutions, we find that the $S_{1.1\mathrm{mm}} > 3.5\,\mathrm{mJy}$ selected 'optically dark' sources make up $\sim 1.7\%$ of the SFRD derived by Madau & Dickinson (2014) at $z = 3.95$.

Due to our flux cut, only sources with $S_{1.1\mathrm{mm}} > 3.5\,\mathrm{mJy}$ have been selected. The found SFRD is thus lower than the SFRD derived by Dudzevičiūtė et al. (2020) using a complete dust-mass-selected sample of SMGs with a flux cut of $S_{870\,\mu\mathrm{m}} \geq 3.6\,\mathrm{mJy}$. They find a $\sim 4$ times higher SFRD of $2.33^{+0.70}_{-0.68} \times 10^{-3}\,\mathrm{M_{\odot}yr^{-1}Mpc^{-3}}$ at $z = 3.95$ using the MAGPHYS estimated redshift for 94% of their sample. We can make an estimate of the Dudzevičiūtė et al. (2020) SFRD with a flux cut of $S_{1.1\mathrm{mm}} \geq 3.5\,\mathrm{mJy}$ by scaling down the SFRD using the differential counts at $850\,\mu\mathrm{m}$ from Geach et al. (2017). We note that this is a crude approximation as there is a relation between redshift and flux density found by Stach et al. (2019) using AS2UDS survey. The found SFRD at $z = 3.95$ is slightly higher than the SFRD found for the $S_{1.1\mathrm{mm}} > 3.5\,\mathrm{mJy}$ selected 'optically dark' sources, indicating that the 10 'optically dark' sources are likely to be similar to the SMGs observed by Dudzevičiūtė et al. (2020). This is also in line with the conclusions from Dudzevičiūtė et al. (2020) as they find that $\sim 17\%$ of their sample is 'optically dark' since they are undetected at $K \gtrsim 25.7$ mag.

As our estimate is only a lower limit to the total contribution of 'optically dark' sources, we also find a much lower contribution than the previous estimate of the contribution of 'optically dark' sources selected from radio observations by van der Vlugt et al. (2023) from the COSMOS-XS survey using the (largely) FIR-based photometric redshifts. To determine the van der Vlugt et al. (2023) SFRD using a similar flux cut as used here, we determine the radio luminosity which corresponds to $S_{1.1\mathrm{mm}} = 3.5\,\mathrm{mJy}$ by finding the $L_{\mathrm{FIR}}$ using the median $870\mu\mathrm{m}/L_{\mathrm{FIR}}$ ratio from AS2UDS. The $L_{\mathrm{FIR}}$ is then converted to $L_{1.4\ \mathrm{GHz}}$ using the radio-FIR correlation from Delvecchio et al. (2021) at $z = 3.95$ (the median redshift of the sample) and assuming a mass of $M_{\star} = 2.8 \times 10^{10} M_{\odot}$ (see Section 5.3.5). We find the flux limit corresponds to $\log_{10} L_{1.4\ \mathrm{GHz}} = 24.2\,\mathrm{W\,Hz^{-1}}$. Integrating the luminosity functions found by van der Vlugt et al. (2023) to this limit, we find a SFRD similar to the SFRD found in this study (albeit with large error bars), as can be seen in Fig. 5.8(b). This confirms the photo-z-based estimates by van der Vlugt et al. (2023) for this subset of sources and suggests that the total contribution of 'optically dark' sources to the SFRD would indeed be similar to the fraction derived by van der Vlugt et al. (2023): $\sim 15^{+7}_{-7}\%$ at $z \sim 5$.

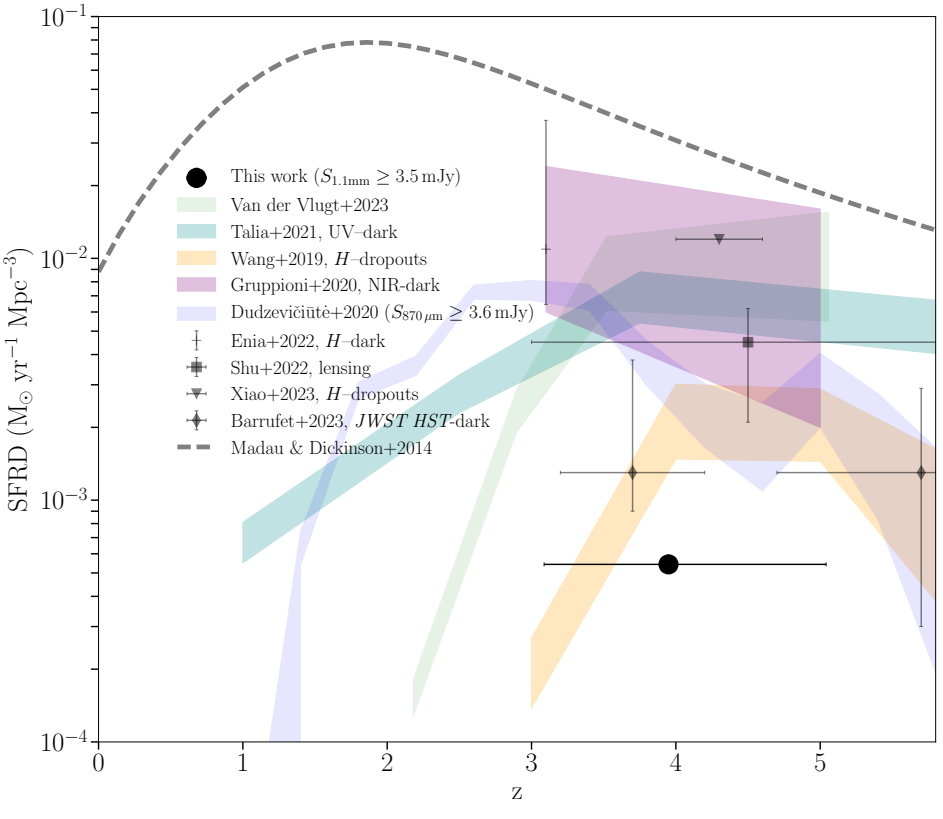


**Figure 5.8:** The cosmic star formation rate density (SFRD) history. The gray dotted curve in both panels represents the study of Madau & Dickinson (2014). The black closed symbol gives the SFRD derived in this study assuming the 'best' redshift for 'optically dark' sources with two redshift solutions. The cyan area and the black point in panel (a) show the SFRD from radio-selected UV–dark galaxies from Talia et al. (2021) and Enia et al. (2022), respectively. The yellow area in panel (a) is the SFRD from the $H$–dropouts in Wang et al. (2019) and the purple region in panel (a) shows the sub-sample of NIR-dark galaxies in the ALPINE fields (Gruppioni et al. 2020). The black square, triangle and diamond in panel (a) give the SFRD from the recent studies by, respectively, Shu et al. (2022), Xiao et al. (2023) and Barrufet et al. (2023). The light green area in both panels shows the SFRD from radio-selected 'optically dark' galaxies from van der Vlugt et al. (2023) where the darker green area in panel (b) gives the SFRD with $S_{870\,\mu\mathrm{m}} \geq 6.3\,\mathrm{mJy}$. The lighter blue area in both panels shows the SMG contribution for a complete dust-mass-selected sample to the SFRD from Dudzevičiūtė et al. (2020) and $S_{870\,\mu\mathrm{m}} \geq 3.6\,\mathrm{mJy}$.

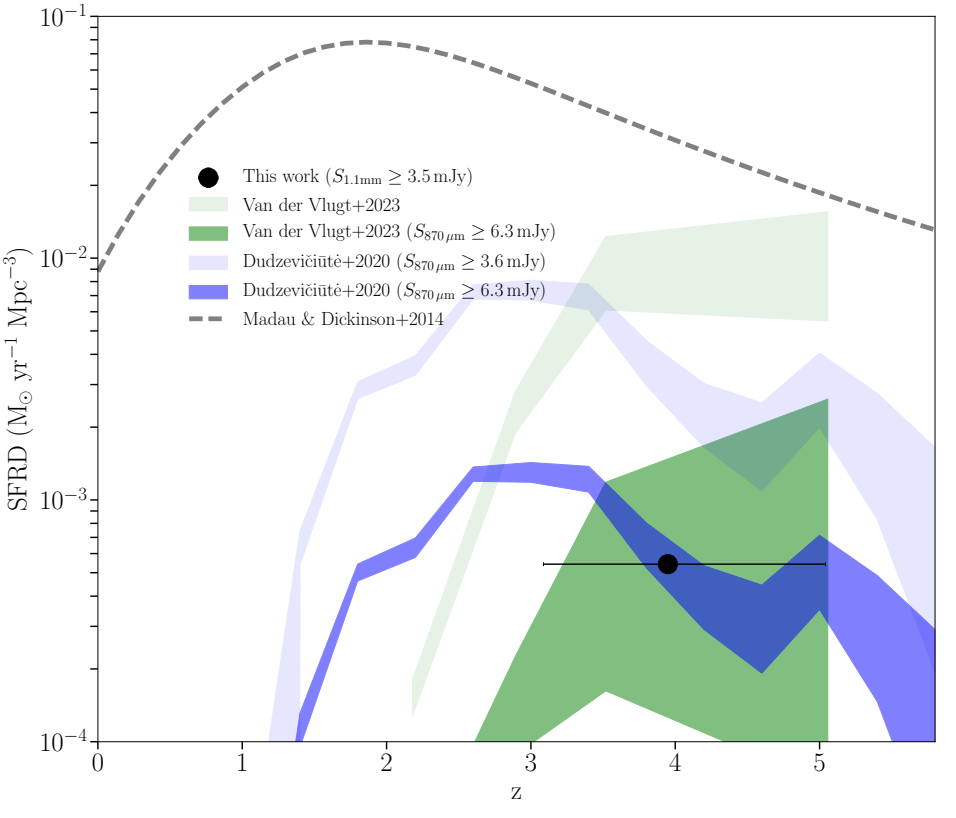


(b)

**Figure 5.8:** Continued. The SFRD contribution with $S_{870\,\mu\mathrm{m}} \geq 6.3\,\mathrm{mJy}$, shown with the dark blue area in panel (b), is found using the relative integrated number counts from Geach et al. (2017).

## 5.5 Summary & Conclusions

We have used ALMA spectral scan observations to obtain spectroscopic redshifts and investigate the properties of 10 'optically dark' galaxies detected in 3 GHz radio observations with counterparts in newly deblended FIR data (Jin et al. in prep.). With the addition of archival and recent additional ALMA observations for two sources, we securely detect the CO(5-4), CO(4-3) and CO(3-2) transitions for eight sources. For the other two sources, we find tentative line detections. We unambiguously identify the redshifts for six sources and for the remaining four sources we find two possible redshift solutions. Using the $L'_{\rm CO(5\text{-}4)}$–$\rm L_{IR}$ correlation, we find the most likely redshift solutions for each source with two redshift solutions. We find that the redshifts of all sources lie between $z = 3.1$ and $z = 5.0$ and have a median redshift of $z = 3.95 \pm 0.62$. Hence all targeted 'optically dark' sources lie at $z \gtrsim 3$.

The derived $\rm L_{IR}$, $L'_{\rm CO(5\text{-}4)}$–$\rm L_{IR}$ correlation and $q_{\rm TIR}$ ratios of the 10 'optically dark' sources all show that these sources have properties that are comparable to SMGs. The comparison between the FIR-SFR determined from SED-fitting and the radio-SFR calculated from the radio flux density shows roughly the same SFR for all sources. Three sources have a slightly elevated radio-SFR compared to the FIR-SFR which could indicate an additional source for the observed radio luminosity in the form of an AGN. We derive that the 'optically dark' sources contribute $5.42 \pm 0.41 \times 10^{-4}\,\rm M_{\odot} yr^{-1} Mpc^{-3}$ to the SFRD at $z \sim 4$. In addition, by integrating the luminosity functions found by van der Vlugt et al. (2023) to the flux limit used to select the 'optically dark' sources ($S_{1.1\rm mm} = 3.5\,\rm mJy$), we determine that the SFRD is in agreement with the SFRD found for the 10 'optically dark' sources. This validates the results derived by van der Vlugt et al. (2023), which relied mostly on photometric redshifts, and confirms the importance of 'optically dark' sources at high redshift ($z > 3$).

## Acknowledgments

The authors wish to thank Mara Salvato for providing us with the COSMOS spectroscopic master catalog. This paper makes use of the following ALMA data: #2022.1.00863.S. ALMA is a partnership of ESO (representing its member states), NSF (USA), and NINS (Japan), together with NRC (Canada), MOST and ASIAA (Taiwan), and KASI (Republic of Korea), in cooperation with the Republic of Chile. The National Radio Astronomy Observatory is a facility of the National Science Foundation operated under cooperative agreement by Associated Universities, Inc. D.vdV. and J.H. acknowledge support of the VIDI research programme with project number 639.042.611, which is (partly) financed by the Netherlands Organisation for Scientific Research (NWO). S.J. is supported by the European Union's Horizon Europe research and innovation program under the Marie Skłodowska-Curie grant agreement No. 101060888. This research made use of ASTROPY, a community developed core Python package for astronomy (Astropy Collaboration et al. 2013, 2018) hosted at http://www.astropy.org/, matplotlib (Hunter 2007), numpy (van der Walt et al. 2011), scipy (Jones et al. 2001), and of TOPCAT (Taylor 2005).

# Appendices

## 5.A ALMA spectra

Here we present the ALMA spectra observed for the 10 targeted sources. Fig. 5.A.1 shows the spectra of sources with one redshift solution and Fig. 5.A.2 to Fig. 5.A.5 show the spectra of sources with two redshift solutions. The spectral configuration uses three frequency tunings to cover 84-108 GHz with a resolution of 7.8 MHz. The three separate tunings cover the frequency range with 5 narrow gaps, indicated with the gray shaded area. The blue dashed line indicates the $1\sigma$ r.m.s. noise for each bin. All lines (detected and tentative) identifications are labeled and line detections are highlighted in green. For sources with two redshift solutions, we show the spectra twice where the possible line transitions for both redshifts are indicated.

## 5.B SED fitting results

Here we present dust SEDs of the 10 galaxies discussed in this work. Fig. 5.A.1 shows the SEDs of sources with one redshift solution and Fig. 5.A.2 to Fig. 5.A.5 show the SEDs of sources with two redshift solutions. For sources with two redshift solutions, we show both SEDs assuming both redshifts. The blue (near-IR wavelengths), red (if present at mid-IR wavelengths) and green (FIR wavelengths) curves represent, respectively, the stellar, mid-infrared AGN (if present) and dust components. Photometries are taken from the new Super-deblended catalog (Jin et al. in prep.) and the ALMA 3mm observations. Arrows mark $3\sigma$ upper limits.

## 5.C Line fitting results

Here we present the Gaussian fits to the CO, [CI](1-0) and H2O($1_{10}$-$1_{01}$) emission lines for the 10 galaxies discussed in this work. Each emission line is plotted in black and centered at the zero velocity corresponding to the redshift of the source. Fig. 5.C.1 shows the fits to the CO(5-4) line, Fig. 5.C.2 shows the fits to the CO(4-3) line, Fig. 5.C.3 shows the fits to the CO(3-2) line, Fig. 5.C.4 shows the fits to the [CI](1-0) line and Fig. 5.C.5 shows the fits to the H2O($1_{10}$-$1_{01}$) line. The Gaussian fits to the lines are shown with red curves. The vertical dashed lines give the measured FWHM.

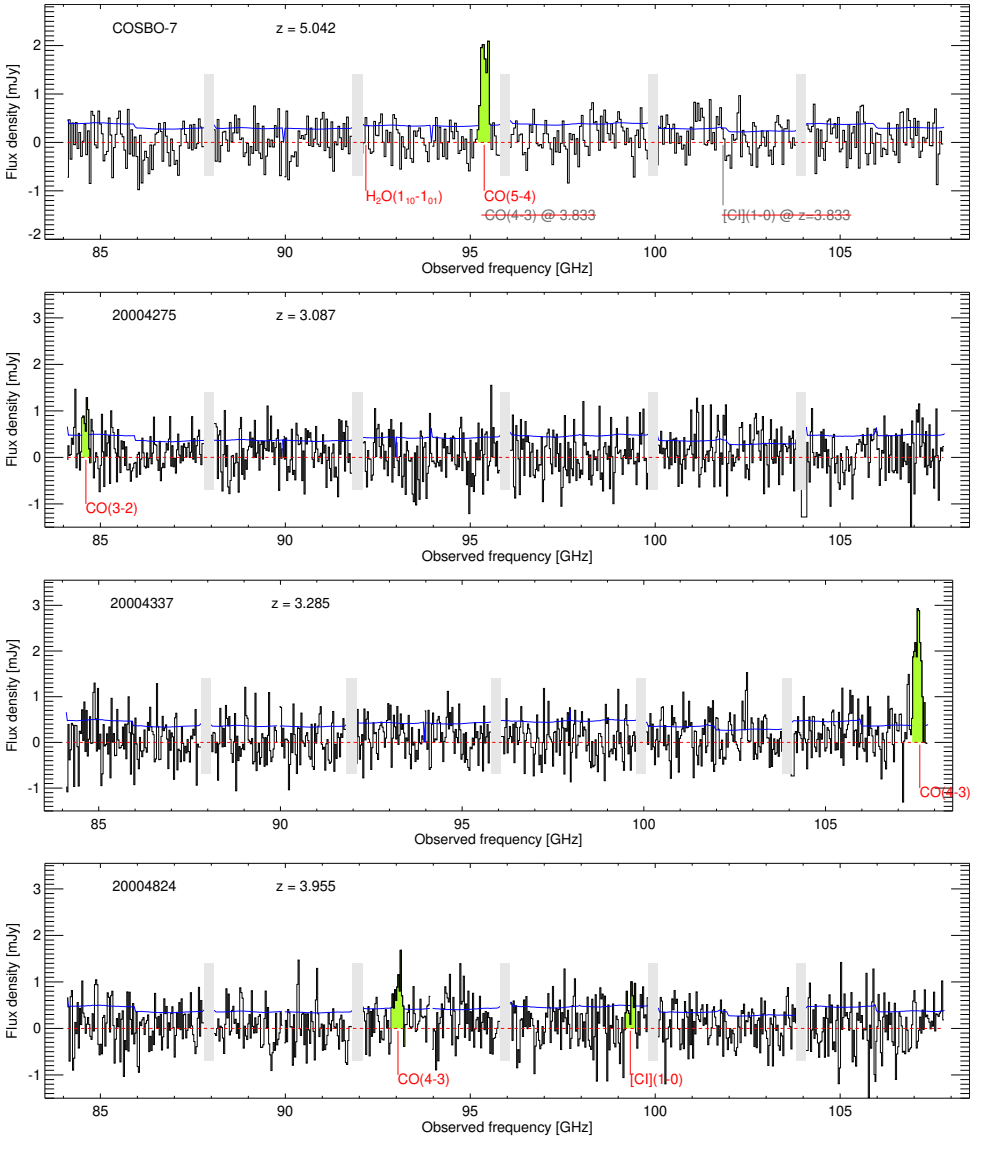


**Figure 5.A.1:** The ALMA Band-3 spectra in the frequency range 84-108 GHz for all sources with one redshift solution. The three separate tunings cover the frequency range with 5 narrow gaps, indicated with the gray shaded area. The emission lines detected are highlighted with green shaded regions and their identifications are labeled.

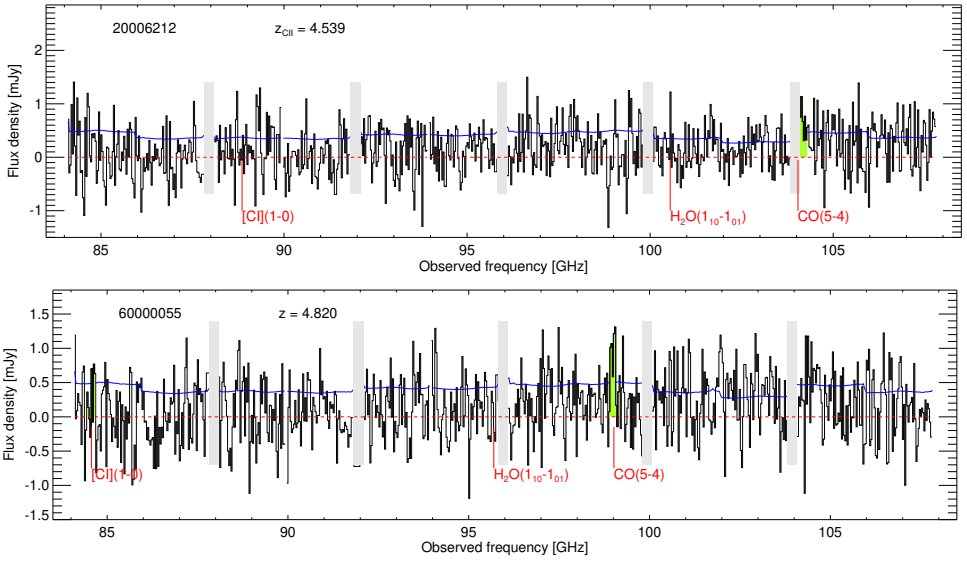


**Figure 5.A.1:** Continued. The line detected for 20006212 is confirmed by a [CII] 158$\mu$m detection in ALMA archival data (ID: 2021.1.00280.L, PI: R. Herrera-Camus). The line detected for 60000055 is confirmed by the recent observations from Sillaseen et al. (in prep.).

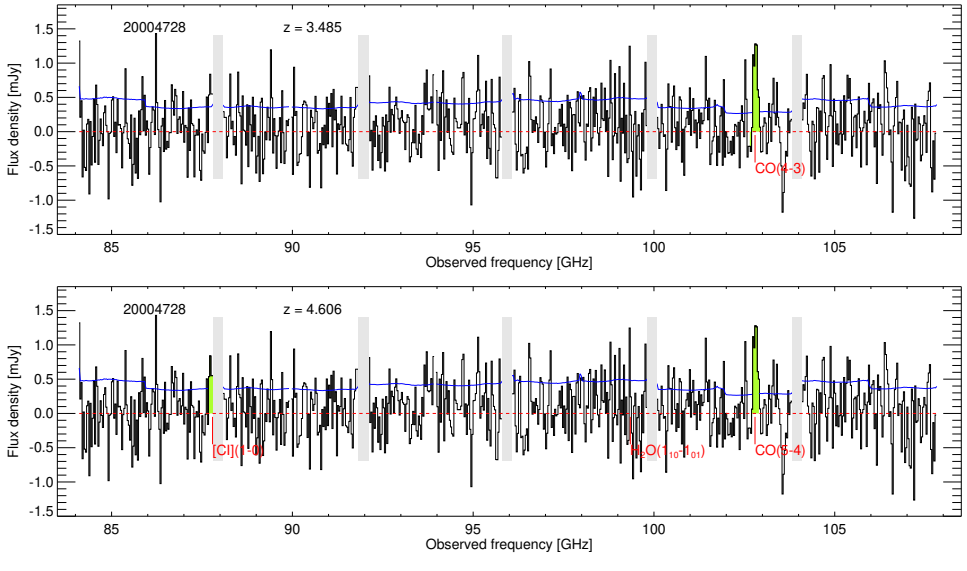


**Figure 5.A.2:** The ALMA Band-3 spectrum for 20004728 in the frequency range 84-108 GHz. This source has two redshift solutions: $z = 3.49$ and $z = 4.61$. The three separate tunings cover the frequency range with 5 narrow gaps, indicated with the gray shaded area. The emission lines detected are highlighted with green shaded regions and their identifications are labeled.

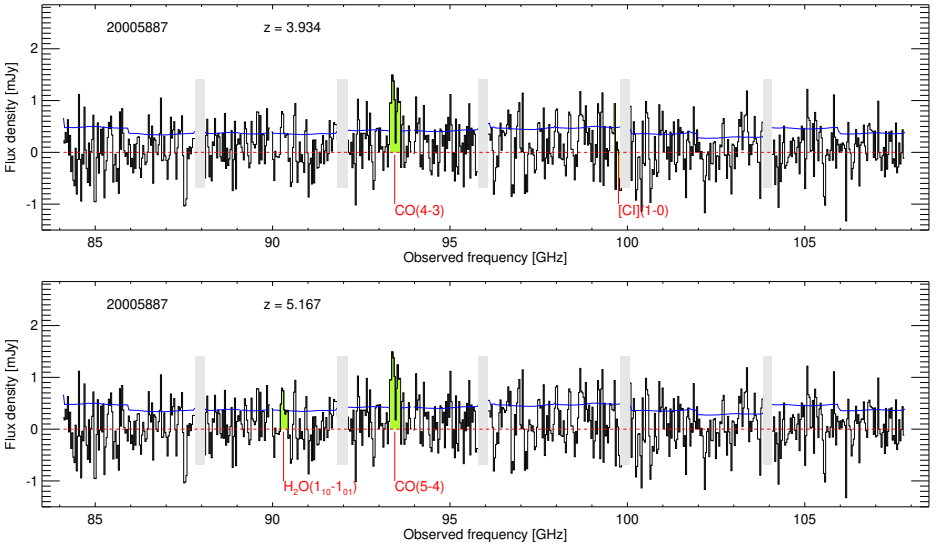


**Figure 5.A.3:** The ALMA Band-3 spectrum for 20005887 in the frequency range 84-108 GHz. This source has two redshift solutions: $z = 3.93$ and $z = 5.17$. The three separate tunings cover the frequency range with 5 narrow gaps, indicated with the gray shaded area. The emission lines detected are highlighted with green shaded regions and their identifications are labeled.

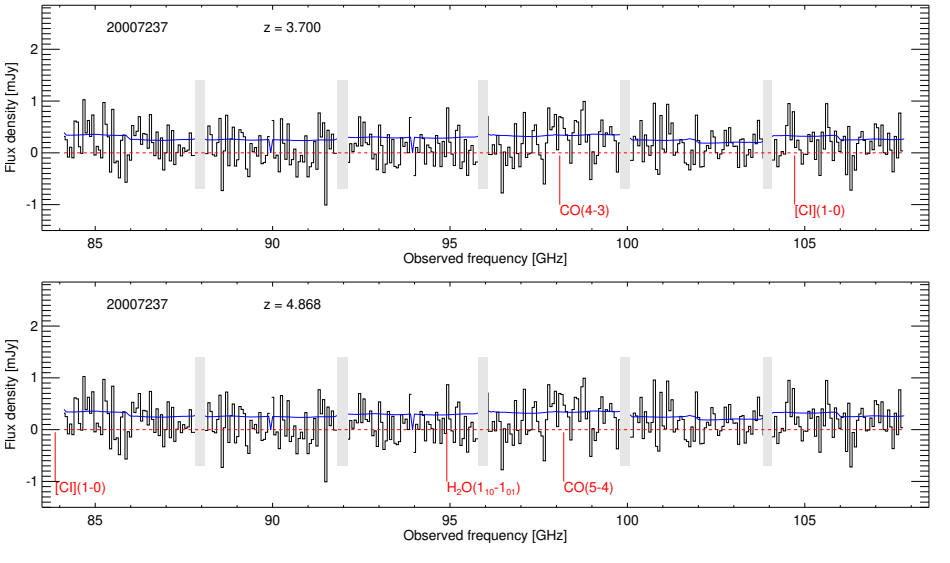


**Figure 5.A.4:** The ALMA Band-3 spectrum for 20007237 in the frequency range 84-108 GHz. The spectrum shows two tentative emission lines at ∼98 GHz and ∼104.5. The source has two redshift solutions: $z = 3.70$ and $z = 4.87$. The three separate tunings cover the frequency range with 5 narrow gaps, indicated with the gray shaded area.

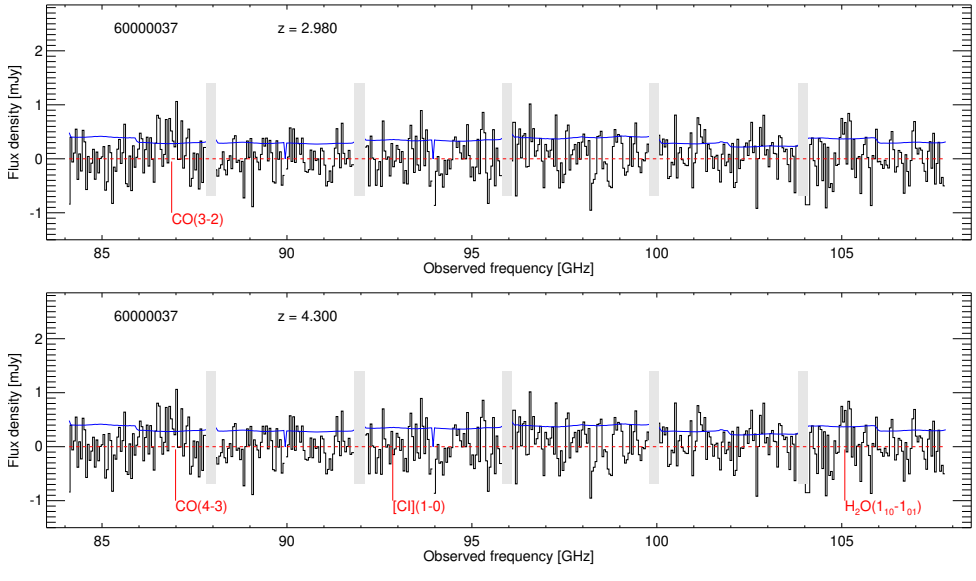


**Figure 5.A.5:** The ALMA Band-3 spectra for 60000037 in the frequency range 84-108 GHz. The spectrum shows two tentative emission lines at ∼86.8 GHz and ∼105 GHz. The source has two redshift solutions: $z = 2.98$ and $z = 4.30$. The three separate tunings cover the frequency range with 5 narrow gaps, indicated with the gray shaded area.

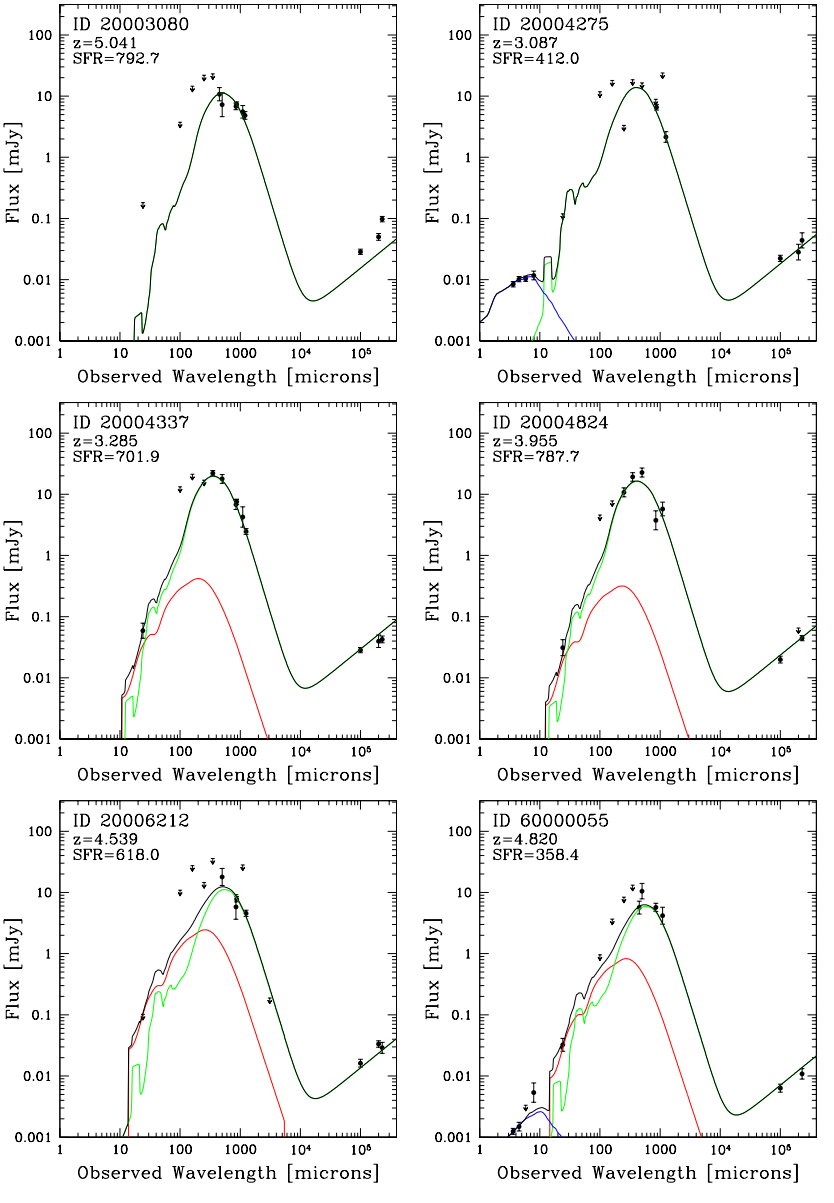




**Figure 5.B.1:** The observed SEDs and its best-fit models for all sources with one redshift solution. The blue (near-IR wavelengths), red (if present at mid-IR wavelengths) and green (FIR wavelengths) curves represent, respectively, the stellar, mid-infrared AGN (if present) and dust components. Photometries are taken from the new Super-deblended catalog (Jin et al. in prep.) and the ALMA 3mm observations. Arrows mark the $3\sigma$ upper limits. The solid curve shows the best fit to the observed SED.

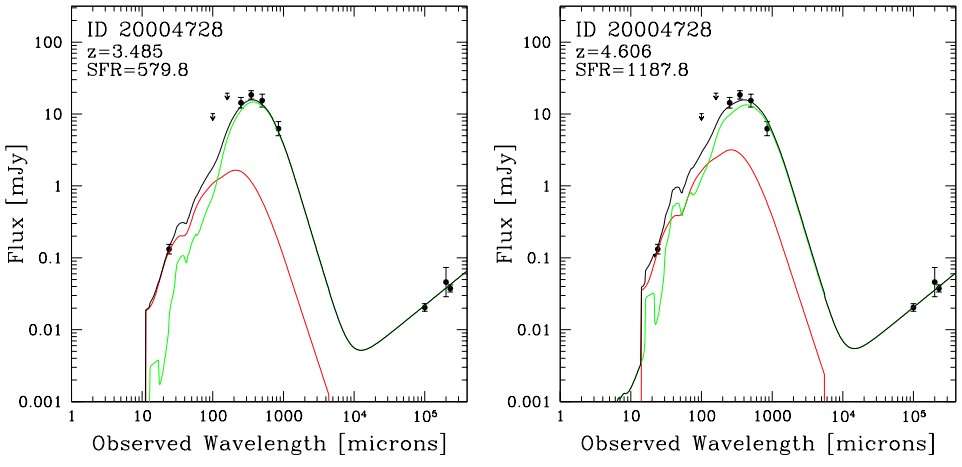


**Figure 5.B.2:** The observed SED and its best-fit model for 20004728. This sources has two redshift solutions: $z = 3.49$ and $z = 4.61$. The blue (near-IR wavelengths), red (if present at mid-IR wavelengths) and green (FIR wavelengths) curves represent, respectively, the stellar, mid-infrared AGN (if present) and dust components. Photometries are taken from the new Super-deblended catalog (Jin et al. in prep.) and the ALMA 3mm observations. Arrows mark the $3\sigma$ upper limits. The solid curve shows the best fit to the observed SED.

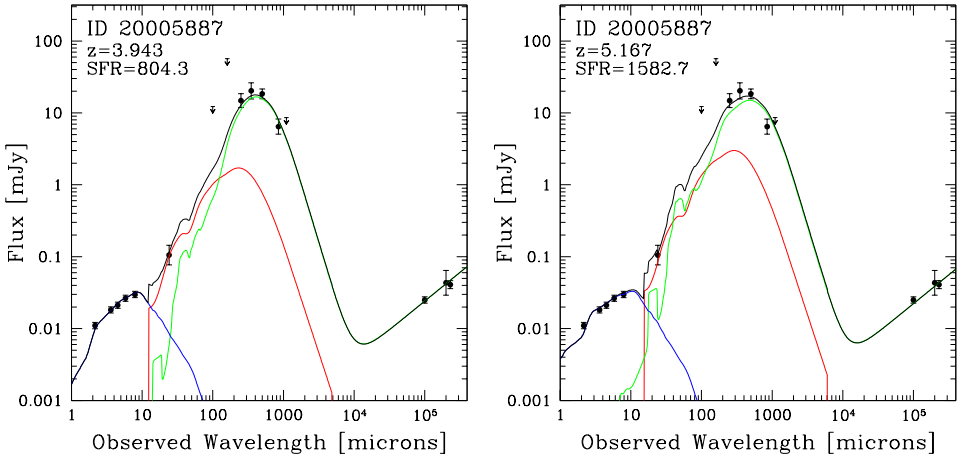


**Figure 5.B.3:** The observed SED and its best-fit model for 20005887. This sources has two redshift solutions: $z = 3.93$ and $z = 5.17$. The blue (near-IR wavelengths), red (if present at mid-IR wavelengths) and green (FIR wavelengths) curves represent, respectively, the stellar, mid-infrared AGN (if present) and dust components. Photometries are taken from the new Super-deblended catalog (Jin et al. in prep.) and the ALMA 3mm observations. Arrows mark the $3\sigma$ upper limits. The solid curve shows the best fit to the observed SED.

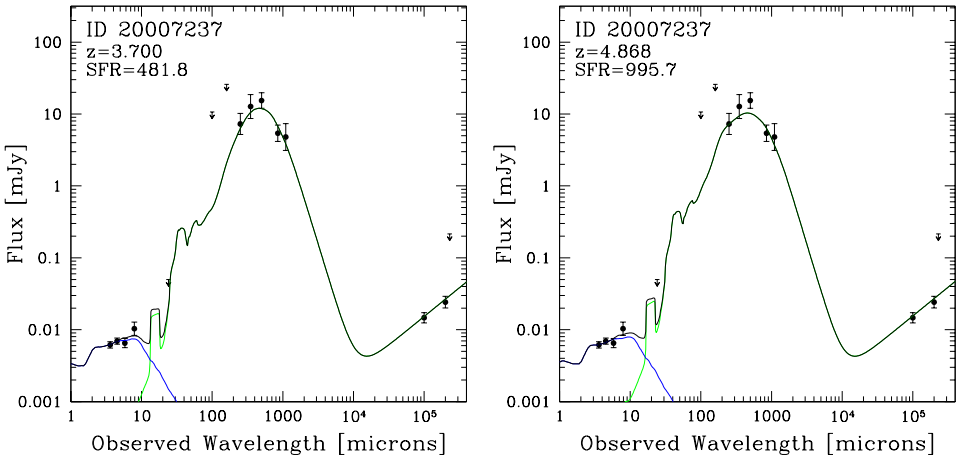


**Figure 5.B.4:** The observed SED and its best-fit model for 20007237. This sources has two redshift solutions: $z = 3.70$ and $z = 4.87$. The blue (near-IR wavelengths), red (if present at mid-IR wavelengths) and green (FIR wavelengths) curves represent, respectively, the stellar, mid-infrared AGN (if present) and dust components. Photometries are taken from the new Super-deblended catalog (Jin et al. in prep.) and the ALMA 3mm observations. Arrows mark the $3\sigma$ upper limits. The solid curve shows the best fit to the observed SED.

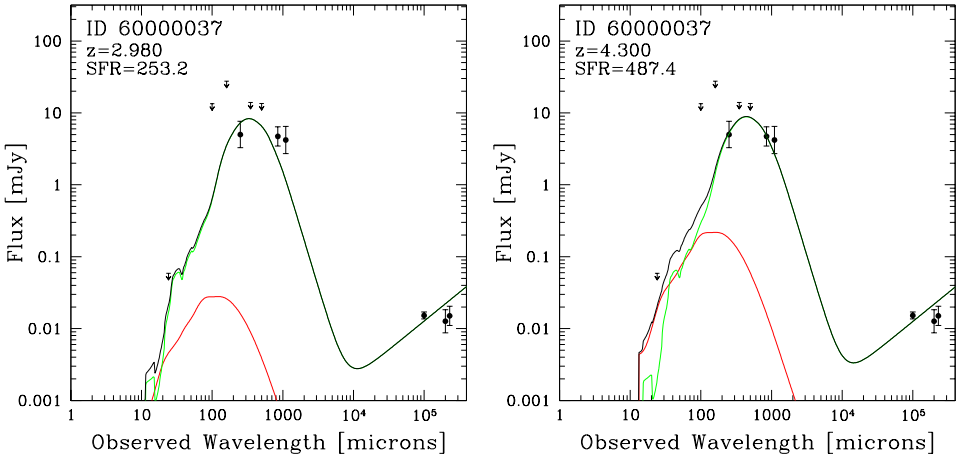


**Figure 5.B.5:** The observed SED and its best-fit model for 60000037. This sources has two redshift solutions: $z = 2.98$ and $z = 4.30$. The blue (near-IR wavelengths), red (if present at mid-IR wavelengths) and green (FIR wavelengths) curves represent, respectively, the stellar, mid-infrared AGN (if present) and dust components. Photometries are taken from the new Super-deblended catalog (Jin et al. in prep.) and the ALMA 3mm observations. Arrows mark the $3\sigma$ upper limits. The solid curve shows the best fit to the observed SED.

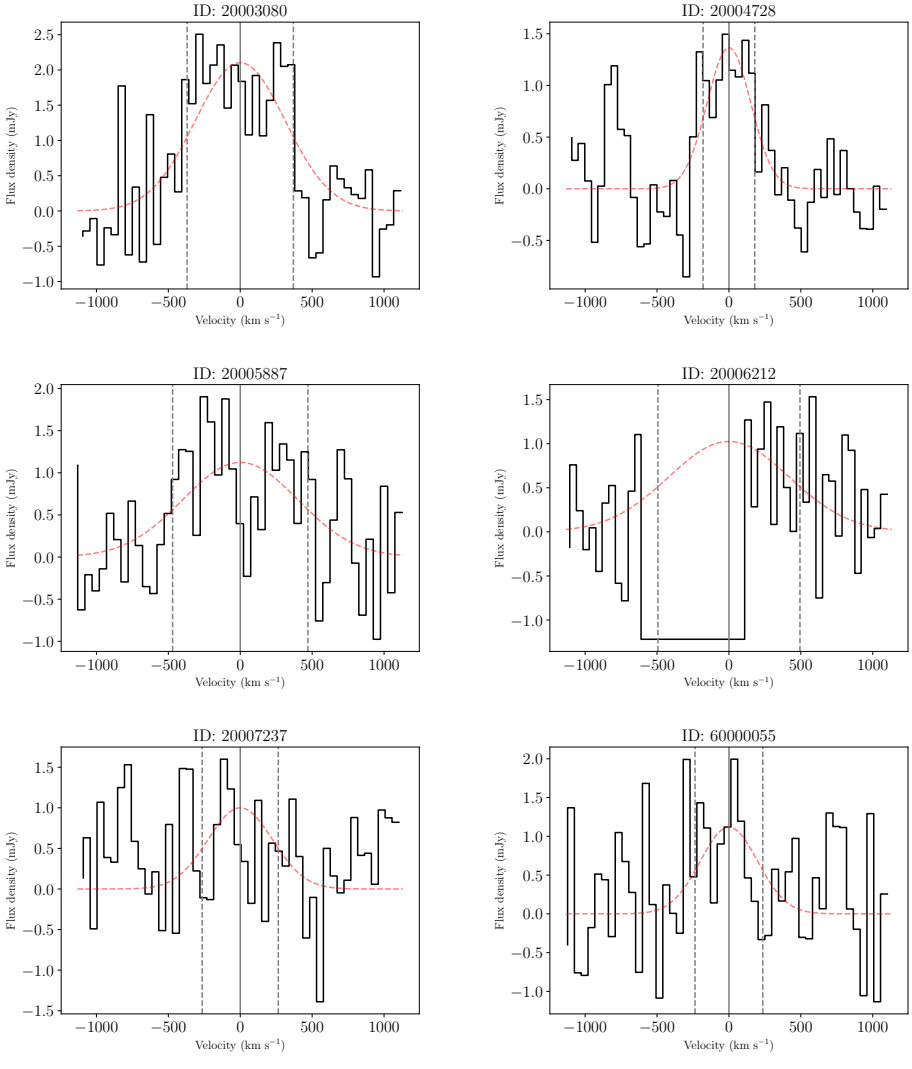


**Figure 5.C.1:** Spectra of the sources with a detected CO(5-4) line (20003080), tentative CO(5-4) line (2000612) and a potential CO(5-4) tentative detection (20007237 and 60000055) or detection (20004728 and 20005887). The velocity is relative to the redshifts of the sources, respectively, 5.041, 4.606, 5.167, 4.539, 4.868 and 4.82 for 20003080, 20004728, 20005887, 2000612, 20007237 and 60000055. The dashed red line gives the Gaussian fitting result. The vertical dashed lines give the measured FWHM.

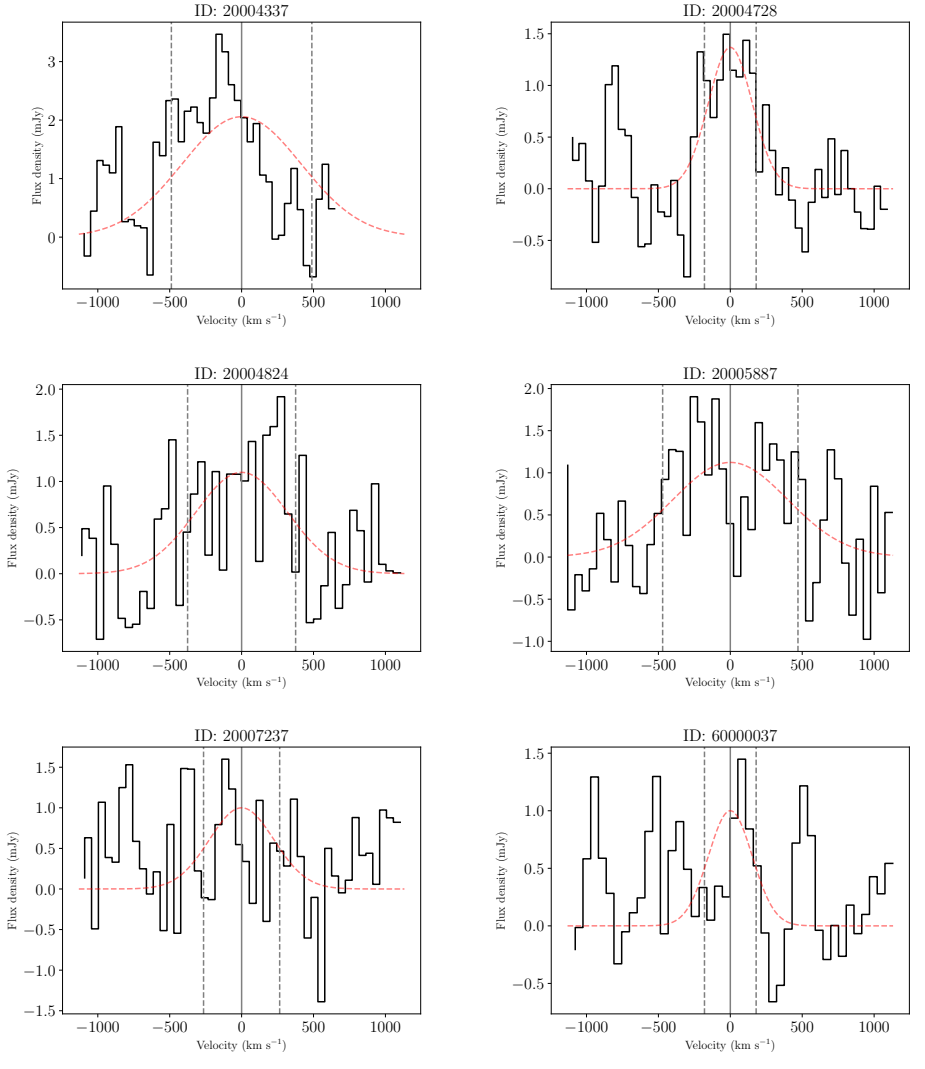


**Figure 5.C.2:** Spectra of the sources with a detected CO(4-3) line profile (20004337 and 20004824) and a potential CO(4-3) tentative detection (20007237 and 60000037) or detection (20004728 and 20005887). The velocity is relative to the redshifts of the sources, respectively, 3.285, 3.485, 3.955, 3.934, 3.7 and 4.3 for 20004337, 20004728, 20004824, 20005887, 20007237 and 60000037. The dashed red line gives the Gaussian fitting result. The vertical dashed lines give the measured FWHM.

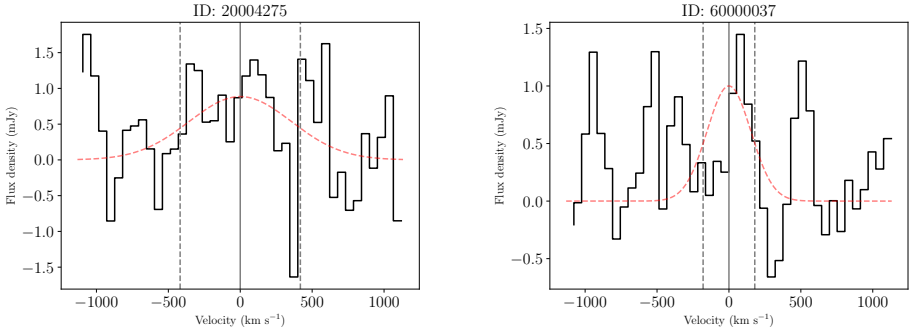


**Figure 5.C.3:** Spectra of the sources with a detected CO(3-2) line (20004275) and a tentative potential CO(3-2) detection (60000037). The velocity is relative to the redshifts of the sources, respectively, 3.087 and 2.98 for 20004275 and 60000037. The dashed red line gives the Gaussian fitting result. The vertical dashed lines give the measured FWHM.

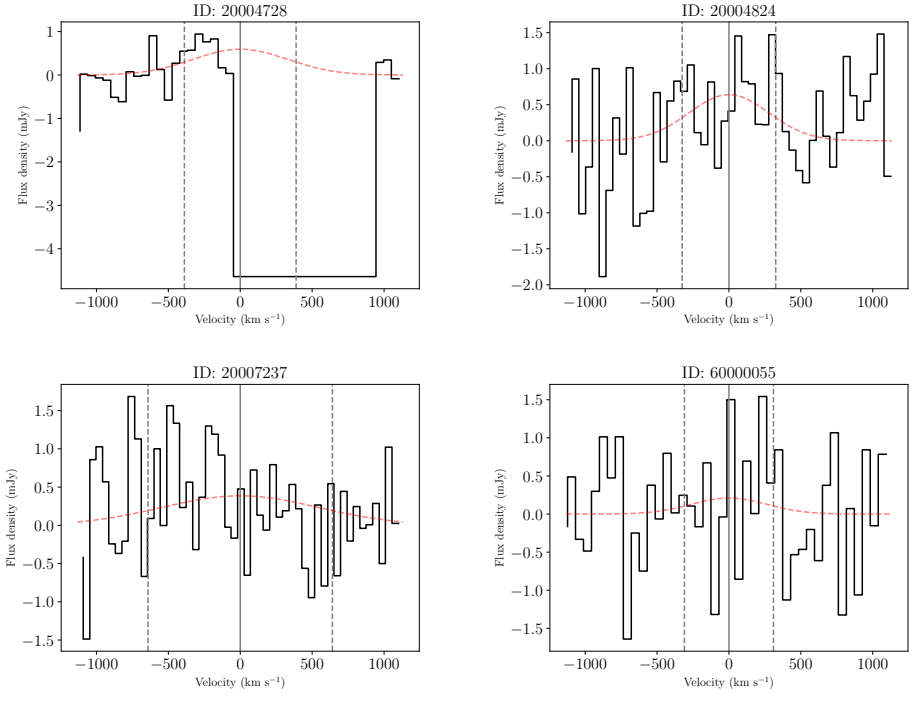


**Figure 5.C.4:** Spectra of the sources with a potential tentative [CI](1-0) line detection. The velocity is relative to the redshifts of the sources, respectively, 4.606, 3.955, 3.7 and 4.3 for 20004728, 20004924, 20007237 and 60000055. The dashed red line gives the Gaussian fitting result. The vertical dashed lines give the measured FWHM.

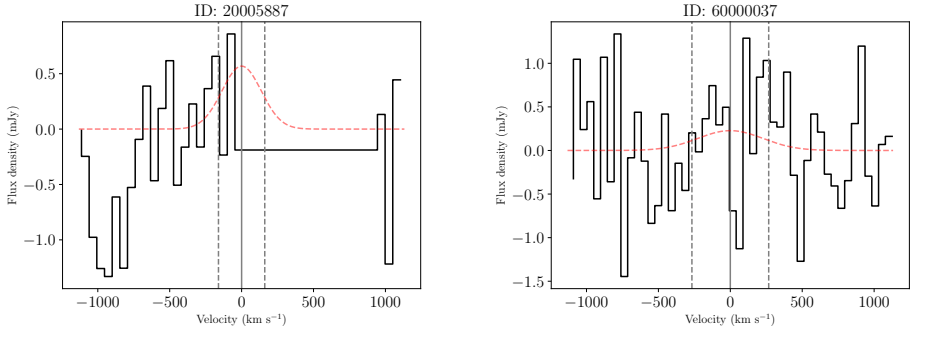


**Figure 5.C.5:** Spectra of the sources with a potential tentative H2O($1_{10}$-$1_{01}$) line detection. The velocity is relative to the redshifts of the sources, respectively, 5.167 and 4.3 for 20005887 and 60000037. The dashed red line gives the Gaussian fitting result. The vertical dashed lines give the measured FWHM.